A Long-Lived Lunar Magnetic Field Powered by Convection in the Core and a Basal Magma Ocean

Saira S. Hamid[1,2], Joseph G. O'Rourke[2], Krista M. Soderlund[3]

ABSTRACT

An internally generated magnetic field once existed on the Moon. This field reached high intensities (~10–100 μT, perhaps intermittently) from ~4.3–3.6 Gyr ago and then weakened to ≲ 5 μT before dissipating by ~1.9–0.8 Gyr ago. While the Moon's metallic core could have generated a magnetic field via a dynamo powered by vigorous convection, models of a core dynamo often fail to explain the observed characteristics of the lunar magnetic field. In particular, the core alone likely may not contain sufficient thermal, chemical, or radiogenic energy to sustain the high-intensity fields for >100 Myr. A recent study by Scheinberg et al. suggested that a dynamo hosted in electrically conductive, molten silicates in a basal magma ocean (BMO) may have produced a strong early field. However, that study did not fully explore the BMO's coupled evolution with the core. Here we show that a coupled BMO-core dynamo driven primarily by inner core growth can explain the timing and staged decline of the lunar magnetic field. We compute the thermochemical evolution of the lunar core with a 1-D, parameterized model tied to extant simulations of mantle evolution and BMO solidification. Our models are most sensitive to four parameters: the abundances of sulfur and potassium in the core, the core's thermal conductivity, and the present-day heat flow across the core-mantle boundary. Our models best match the Moon's magnetic history if the bulk core contains ~6.5–8.5 wt% sulfur, in agreement with seismic structure models.

[1] Corresponding author sshamid1@asu.edu
[2] School of Earth and Space Exploration, Arizona State University, Tempe, AZ 85287, USA
[3] Institute for Geophysics, Jackson School of Geosciences, University of Texas at Austin, Austin, TX 78758, USA

1. INTRODUCTION

Paleomagnetic analyses of lunar meteorites and Apollo samples suggest that a high-intensity magnetic field of ~10–100 μT existed ~4.25–3.56 billion years (Gyr) ago, followed by a weakened field of ≲ 5 μT that persisted until ~1.9–0.8 Gyr ago (e.g., Tikoo et al. 2014, Tikoo et al. 2017, Mighani et al. 2020, Strauss et al. 2021, Wieczorek et al. 2022). Generation of an intrinsic magnetic field via dynamo action requires vigorous motion of an electrically conducting fluid such as the liquid portion of a metallic core (e.g., Bullard 1949, Elsasser 1950, Bullen 1954, Glatzmaier and Roberts 1995, Kageyama et al. 1995). Various observations indicate that the Moon has a metallic core, including seismic data from the Apollo missions (e.g., Garcia et al. 2011, Weber et al. 2011), electromagnetic sounding (e.g., Hood et al. 1999, Shimizu et al. 2013), and gravity data from the Gravity Recovery and Interior Laboratory (GRAIL) mission (e.g., Williams et al. 2014), which are all consistent with a core radius of ~250–430 km. Today, a solid inner core with a radius up to ~250 km may also exist (Williams et al. 2014, Weber et al. 2011).

Models of the thermal evolution of the lunar core have difficulty reproducing the history of the lunar magnetic field (e.g., Evans et al. 2018, Laneuville et al. 2014, Scheinberg et al. 2015). These models have two goals that often seem incompatible: 1) sustaining a long-lived field (e.g., multiple Gyr) and 2) sustaining an early strong field (i.e., >10 μT, at least for the first ~1 Gyr). With available energy sources internal to the core (e.g., radiogenic, latent, and chemical energy, plus inner core precession), the Moon can sustain a low-intensity field for long durations (e.g., Laneuville et al. 2014; Scheinberg et al. 2015, Evans et al. 2018, Stys & Dumberry 2020). However, Evans et al. (2018) showed that those energy sources could only sustain a >10 μT field for <50 Myr, assuming that the radius of the core is ≤380 km as favored by Weber et al. (2011) and Williams et al. (2014). So, sustaining a >10 μT field for ~1 Gyr is highly improbable without an external mechanism, such as mechanical stirring between the solid mantle and the liquid core from precession of the lunar spin axis (e.g., Dwyer et al. 2011; Meyer & Wisdom 2010; Ćuk et al. 2019) and/or impact-induced changes in the rotation rate of the solid mantle (e.g., Le Bars et al. 2011). Another solution to this seeming paradox is to invoke intermittency during the high-intensity epoch. For example, a recent study proposed that foundering of relatively cold material in the lunar mantle may have excited episodes of

rapid core cooling that lasted <1 Myr (Evans & Tikoo 2022). Finally, in this study, we explore the idea that the core is not the only potential host for a lunar dynamo as argued by Scheinberg et al. (2018).

1.1. A Basal Magma Ocean

Almost any scenario for the formation of the Moon involves enough energy to melt much of the newly formed Moon (e.g., Hartmann & Davis 1975, Warren 1985, Elkins-Tanton et al. 2011, Canup 2012, Ćuk & Stewart 2012, Nakajima & Stevenson 2014). The resulting magma ocean is often modeled as solidifying in three primary stages (e.g., Elardo et al. 2011, Wieczorek et al. 2006, Hess & Parmentier 1995, Hamid & O'Rourke 2022). As the lunar magma ocean cooled, dense mafic cumulates (e.g., olivine and pyroxene) formed and sank towards the bottom. Once most of the lunar magma ocean solidified, anorthositic plagioclase with lower density began to crystallize, rising to form the lunar crust. The final, highly evolved liquids, "ur-KREEP" (enriched in uranium, thorium, potassium, rare earth elements, and phosphorus), alongside ilmenite-rich cumulates, would be gravitationally unstable because of their high densities. Some fraction of this ur-KREEP-ilmenite mixture eventually sank to the base of the mantle, ponding as a layer above the core-mantle boundary (CMB). Radiogenic heat from elements present in this fallen ur-KREEP layer, such as uranium, thorium, and potassium (with concentrations up to ~12 times higher than the bulk mantle), could fully melt this layer (e.g., Scheinberg et al. 2018). The result is a basal magma ocean (BMO) that persists until convective heat loss into the overlying mantle causes solidification. The nominal model of Scheinberg et al. (2018) had a 301-km peak thickness BMO; less conservative models had BMO thicknesses up to 450 km.

Models are equivocal about the lifetime of a BMO. For example, a small compositional density contrast between the BMO and the overlying mantle could make the BMO short-lived (Stegman et al. 2003). In this scenario, thermal expansion of the BMO can overcome the compositional density contrast between the BMO and the overlying mantle, causing the BMO to buoyantly rise and re-mix with the mantle. Conversely, the persistence of interstitial fluid trapped within the solidified cumulates could leave the BMO sequestered at the CMB (Elkins-Tanton et al. 2011, Scheinberg et al. 2018). Indeed, interpretations of geophysical data (Khan et al. 2014), seismic data (Weber et al. 2011), and gravity data (Williams et al. 2014) have indicated that a

deep-seated zone of partial melt at the CMB may exist today. This partial melt could be the last remnant of a once-thicker BMO.

The lunar BMO could have sustained a dynamo if it was vigorously convecting and had an electrical conductivity, σ, of several thousand S/m (Scheinberg et al. 2018). Such a BMO dynamo would have an advantage over the core in terms of generating strong crustal fields because it is closer to the surface (e.g., Ziegler & Stegman 2013). Magnetic fields attenuate rapidly with distance, so a magnetic field generated in the BMO would appear stronger at the surface than a magnetic field generated with the same strength in the core (e.g., Scheinberg et al. 2018, Stevenson 1983, Christensen 2010). While sufficiently high conductivity is a challenge for this hypothesis, thermal coupling between the BMO and core can fortunately be explored regardless of this uncertainty.

Our study is built on the whole-Moon models presented in Scheinberg et al. (2018). That study focused on the thermal evolution of the solid mantle and BMO to explain the early, strong (i.e., >10 μT) lunar dynamo. Both the BMO and the core were assumed to be well-mixed on the timescales of the overlying solid mantle convection and to have an adiabatic temperature gradient, except during the phase in which the magma ocean increases in temperature. That study further tested the sensitivity of their model to the reference viscosity in the solid mantle, the fraction of the KREEP layer that remained near the surface, and the fraction of radioactive material concentrated in the BMO. At the start of their simulations, the BMO exhibited a rapid increase in heat flow from radiogenic heating, followed by a steady decline to its solidus temperature. A detailed model of the core was not included because the core is relatively small and does not strongly affect the thermal evolution of the BMO and solid mantle. In this study, we do not directly model the BMO-hosted dynamo, but rather focus on the core to test if models of lunar evolution that feature a BMO as a boundary condition can explain both the strong, early dynamo and the later dynamo that produced much weaker fields (Figure 1).

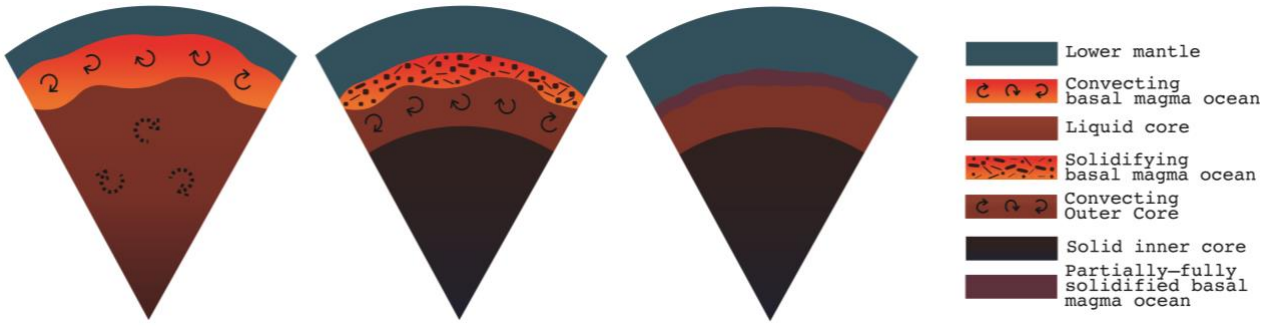

Figure 1: We study three stages in the coupled evolution of the lunar BMO and core. (Left) Convection in the BMO with the potential to produce an early, high intensity dynamo ~4.25–3.56 Gyr ago while the core was fully liquid. Dashed arrows indicate that in limited scenarios, thermal convection in the core may have occurred in tandem with the BMO-hosted dynamo. (Middle) Compositional convection in the core produced a late, low intensity dynamo until ~1.9–0.8 Gyr ago once the inner core started growing and the BMO began to solidify. (Right) The internal field ceased ~1 Gyr ago once the BMO solidified sufficiently, the inner core grew too large, and convection ceased in the liquid outer core.

2. METHODS

2.1. Structure of the Metallic Core

We assume that the lunar core is an iron alloy that starts fully liquid with no chemical or thermal stratification. To build our models, we assume that sulfur is the major light element in the core, given its siderophile behavior and cosmochemical abundance (e.g., Pommier et al. 2018, Cameron 1973). Our models also include trace amounts of potassium as a source of radiogenic heating. Other studies have speculated about the possible roles of other light elements in the lunar core, including carbon (e.g., Dasgupta et al. 2009), silicon (e.g., Berrada et al. 2020), and phosphorous (e.g., Yin et al. 2019). However, the complexities of a core with multiple light elements are beyond the scope of this study.

A 1-D, parameterized description of the structure of the core is the foundation of our models. As described in Appendix A, we used hydrostatic equilibrium and equations of state detailed in Khan et al. (2017) to calculate the radial profiles of density, pressure, temperature, and gravitational acceleration within the core. Our fiducial structural model assumes that the core contains 6 wt% sulfur and has a central pressure and temperature of 5.15 GPa and 1800 K, respectively, to match the core parameters described in Scheinberg et al. (2018). The radius of the core is then 350 km, which is also the same as in Scheinberg et al. (2018) and in agreement with available observational constraints. However, Scheinberg et al. (2018) used an average density for the core appropriate to a composition

of pure iron, which would increase the total mass of the core by ~20%. Fortunately, most of the structural parameters that are key to our thermodynamic calculations (e.g., K_0, K_1, L_ρ, and A_ρ in Table D1) are not sensitive to the bulk composition of the core. Sulfur is most important to the thermal evolution of the lunar core via its effect on the bulk liquidus. Using a fixed sulfur content to calculate other parameters (e.g., ρ_0, P_0, and M_C) should only introduce inaccuracies that are smaller than the observational uncertainties.

2.2. Energetics of the Metallic Core

The overlying BMO controls the evolution of the core. In the models of Scheinberg et al. (2018), the BMO is initially set to 1700 K at 4.2 Ga, heats up for ~200 Myr due to radiogenic heating, and subsequently cools until it reaches the initial temperature when the models are stopped. We start tracking the evolution of the core at the time when the BMO starts cooling again. At that time, we assume the core is fully molten and has an adiabatic temperature gradient throughout. We set that "initial" temperature at the top of the core equal to that at the bottom of the BMO. From the results of Scheinberg et al. (2018), we know the total heat flow across the core-mantle boundary (Q_{CMB}) over time:

$$Q_{CMB} = Q_B - Q_{S_{BMO}} - H_{BMO} \quad (1)$$

Here, Q_B is the heat flow outward from the BMO into the solid mantle, $Q_{S_{BMO}}$ is heat associated with secular cooling, and H_{BMO} is the radiogenic heating in the BMO. In order to model the magnetic history of the Moon until present day (i.e. after the BMO model has stopped), we further assume that Q_{CMB} changes linearly to a specified present day value, which could be the same or (much) less than the value of Q_{CMB} when the BMO solidifies. With the boundary condition provided by the BMO model, we then use a well-established method, developed to study Earth's core (e.g., Labrosse 2015), to model the thermodynamic evolution of the lunar core once it starts cooling again. First, we can calculate the global heat budget of the core:

$$Q_{CMB} = Q_L + Q_G + Q_R + Q_S \quad (2)$$

Here, Q_S represents the secular cooling of the core and is proportional to the core's specific heat. We assume that trace amounts of potassium produce radiogenic heating (Q_R). The remaining two terms are only relevant once the inner core nucleates: energy from latent heat (Q_L) and gravitational energy

from the exclusion of light elements into the outer core (Q_G) that are released as the inner core grows.

Given the total heat flow, we solve for the rate of change in the CMB temperature. As shown in Appendix B, most of the terms on the right side of equation (2) are products of dT_{CMB}/dt and a term $(\tilde{Q})$ that depends only on the thermodynamic properties of the core and its structural parameters. Each of those terms is calculable using polynomial functions. We can thus rearrange equation (2):

$$\frac{dT_{CMB}}{dt} = \frac{Q_{CMB} - Q_R}{\widetilde{Q_S} + \widetilde{Q_G} + \widetilde{Q_L}} \quad (3)$$

The growth rate of the inner core is directly proportional to dT_{CMB}/dt also (see Appendix B). Because equation (2) does not include any secular cooling of the inner core, we are implicitly assuming that the inner core is perfectly insulating (i.e., with zero thermal conductivity). We could also model a conductive inner core with infinite thermal conductivity, but the associated heat flow is a minor contribution to the global heat budget if the inner core extends to only <75% of the core radius, as expected at present day. Technically, equations (2) and (3) are only valid if the liquid portion of the core is convective and thus maintaining a nearly adiabatic thermal profile. This assumption is not valid at present day since thermal stratification probably exists since the core heat flux was likely lower than the heat flux that can be conducted along the adiabat for most of the Moon's evolution (e.g., Laneuville et al. 2014).

Our models use a liquidus for the core that depends on the bulk composition. We adapted Equation 29 from Buono & Walker (2011), in which the Fe-FeS liquidus is fit to a polynomial that is fourth-order in both pressure and sulfur content. Our model uses an approximation of the liquidus that is first-order in both pressure and sulfur content. Specifically, we estimated the approximate pressure derivative (dT_L/dP) based on the difference in the liquidus temperatures at 5.15 GPa at the center of the core versus 4.43 GPa at the CMB for 6 wt% sulfur. We found the approximate compositional derivative (dT_L/dc) based on the difference in liquidus temperatures for 0 vs. 25 wt% sulfur at 5 GPa (Table D1).

2.3. Strength of a Core-Hosted Dynamo

Vigorous convection in the core can produce a dynamo through the conversion of kinetic to magnetic energy. In general, there are two types of

power sources for convection in the core. First, the buoyancy of light elements released from inner core solidification can drive compositional convection. Second, thermal buoyancy from secular cooling of the core, freezing of the inner core, and/or radiogenic heating can power thermal convection. For thermal convection to occur from secular cooling alone, Q_{CMB} must exceed the adiabatic heat flow (Q_{AD}), which equals the product of the thermal conductivity of the core and the adiabatic temperature gradient (see Appendix B). Once the inner core nucleates, the critical heat flow above which convection occurs is lowered.

We combined the energy and entropy budgets for the core to calculate the total dissipation available to power a dynamo (e.g., Labrosse 2015):

$$\Phi_{CMB} = \Phi_L + \Phi_G + \Phi_R + \Phi_S - \Phi_K. \quad (4)$$

Here, Φ_L, Φ_G, Φ_R, and Φ_S are the dissipation terms associated with Q_L, Q_G, Q_R, and Q_S, respectively. The last term (Φ_K) corresponds to the entropy sink associated with thermal conduction in the core. Appendix B contains the polynomial expressions for each dissipation term, which, like the energy terms, depend on the thermophysical properties of the core and its overall cooling rate. Critically, we assume a dynamo exists if the dissipation is positive (i.e., if $\Phi_{CMB} > 0$ W). This criterion yields similar predictions as another often-used criterion, which is that the magnetic Reynolds number (defined below) exceeds a critical value of 50–100 (e.g., Roberts 2007).

Several scaling laws are available to convert the dissipation (in Watts) into the strength of the magnetic field at the equatorial surface of the Moon (in Teslas). First, we use a scaling law based on core energetics (see Appendix B) to calculate the total dipole moment (D_M) of the Moon (units of A m^2). In this case, assuming the lunar magnetic field is dipolar, the surface field strength at the magnetic equator is

$$B = \frac{\mu_0 D_M}{4\pi R_M^3}, \quad (5)$$

where R_M is the radius of the Moon and μ_0 is the permeability of free space. Additionally, we estimate the magnetic field intensity using three scaling laws that relate the associated convective power to the anticipated convective velocities (e.g., Christensen 2010). These scaling laws use different force balances to calculate the strength of the magnetic field in the core (B_C). First, mixing length theory (ML) assumes a balance between inertial and buoyancy forces:

$$B_{ML} = \left[2c\mu_0(\rho_0 R_C^2 \Phi_{CMB}^2)^{\frac{1}{3}}\right]^{\frac{1}{2}}, \quad (6)$$

where $c \sim 0.63$ is a constant of proportionality, ρ_0 is the central density in the core, and R_C is the radius of the core. Second, assuming a balance of Coriolis, inertial, and gravitational (Archimedes) (CIA) forces yields:

$$B_{CIA} = \left[2c\mu_0(\rho_0^2 R_C^4 \Omega \Phi_{CMB}^3)^{\frac{1}{5}}\right]^{\frac{1}{2}}, (7)$$

where Ω is the present-day angular velocity of the Moon, which may underestimate the field strength since the Moon likely rotated faster in the past. Third, the Magneto-Archimedes-Coriolis (MAC) scaling assumes a balance between Lorentz, gravitational, and Coriolis forces:

$$B_{MAC} = \left[2c\mu_0(\rho_0 R_C^2 \Omega \Phi_{CMB})^{\frac{1}{2}}\right]^{\frac{1}{2}}. (8)$$

With these three scaling laws, we calculate the surface field strength of the dipole component as

$$B_S = \frac{1}{7} B_C \left(\frac{R_C}{R_M}\right)^3. (9)$$

The ratio of the Moon's core radius to the Moon's radius (R_M) accounts for the fact that the dipole field at the surface is smaller than the dipole field at the core (Scheinberg et al. 2018). The pre-factor of 1/7 assumes an Earth-like power spectrum for the magnetic field and accounts for the fact that not all of the energy in the magnetic field is partitioned into the poloidal components that can reach the surface (e.g., Christensen et al. 2009, Scheinberg et al. 2018). Note that the core field is assumed to diffuse across an electrically insulating mantle in this approach, thus neglecting the contribution of the BMO. Because the BMO is argued to have a relatively large electrical conductivity, our surface field strength calculations may be considered as lower-bound estimates (discussed further in section 4.3).

2.4. Local Rossby Number

We further assess the dipolarity of the Moon's magnetic field, particularly whether a dipole-dominated or multipolar dynamo may be preferred. Although there are numerous hypotheses for what controls the breakdown of the dipole (e.g., Soderlund & Stanley 2020), we consider here the local Rossby number:

$$Ro_l = \frac{U}{2\,\Omega\, l}, \quad (10)$$

where $\Omega = 2\pi/T$ is the angular velocity of the Moon, T is the rotation period in seconds, l is the characteristic length scale of the flow, and U is the characteristic fluid velocity. This dimensionless parameter measures the

relative importance of inertial to Coriolis forces at convective length scales. Numerical models of planetary dynamos indicate that dipole-dominated solutions tend to be found approximately when $Ro_l < 0.1$ (i.e., when inertial effects are relatively weak compared to rotation), with multipolar solutions occurring for larger Ro_l values (e.g., Christensen & Aubert 2006).

In order to estimate this parameter, we assume a characteristic fluid velocity and length scale following scaling law predictions as done for the magnetic field strengths (e.g., Christensen 2010). The mixing length (ML) scaling yields

$$U_{ML} = \left(\frac{\Phi_{CMB} R_C}{\rho_0}\right)^{\frac{1}{3}}, \quad l_{ML} = R_C, \quad Ro_{l,ML} = \left(\frac{\Phi_{CMB} R_C}{\rho_0}\right)^{\frac{1}{3}} (2\,\Omega\,R_C)^{-1}, \tag{11}$$

the Coriolis, inertial, and gravitational (Archimedes) (CIA) scaling yields

$$U_{CIA} = \left(\frac{\Phi_{CMB}}{\rho_0}\right)^{\frac{2}{5}} \left(\frac{R_C}{\Omega}\right)^{\frac{1}{5}}, \quad l_{CIA} = \left(\frac{U_{CIA}\,R_C}{\Omega}\right)^{\frac{1}{2}}, \quad Ro_{l,CIA} = \left(\frac{\Phi_{CMB}}{\rho_0}\right)^{\frac{2}{5}} \left(\frac{R_C}{\Omega}\right)^{\frac{1}{5}} (4\,\Omega\,U_{CIA}\,R_C)^{-\frac{1}{2}}, \tag{12}$$

and the Magneto-Archimedes-Coriolis (MAC) scaling yields

$$U_{MAC} = \left(\frac{\Phi_{CMB}}{\rho_0 \Omega}\right)^{\frac{1}{2}}, \quad l_{MAC} = R_C \quad Ro_{l,MAC} = \left(\frac{\Phi_{CMB}}{\rho_0 \Omega}\right)^{\frac{1}{2}} (2\,\Omega\,R_C)^{-1}. \tag{13}$$

Here, $\phi = \Phi_{CMB} / V_{OC}$ is the volumetric thermodynamically available power over the fluid core. We could also use these velocity scalings to confirm that the magnetic Reynolds number, which relates the Ohmic diffusion timescale to the convective timescale, exceeds the critical value of ~50 for magnetic field generation to occur (e.g., Roberts 2007). With the definition

$$Re_m = \mu_0 \sigma U l, \tag{14}$$

a flow velocity faster than ~0.1–1 mm/s produces $Re_m > 50$ if we assume the length scale is equal to the core radius and the electrical conductivity is σ ~10^5 to 10^6 S m^{-1} (e.g., Berrada et al. 2020, Pommier et al. 2020).

2.5. Model Parameters

Our model ingests the BMO model outputs from Scheinberg et al. (2018) and calculates the energy and dissipation budgets for the core to determine when the core may host a dynamo (see Table D2). Following the nomenclature of Scheinberg et al. (2018), naming of the BMO models corresponds to the parameters chosen to describe the mantle and the initial solidification of its magma ocean. For example, 'V19' indicates a reference mantle viscosity of 10^{19} Pa s, 'K50' indicates that 50% of the KREEP layer remained trapped near the surface, and 'p54' indicates that 54% of the internal radiogenic heating

occurs in the sunken KREEP material. We focus on the BMO models that generate magnetic fields with lifetimes of <2.9 Gyr for consistency with the paleomagnetic record (e.g., Mighani et al. 2020). We adopt the nominal BMO case, V19K50p54, as the basis for our nominal model of the core as it assumes moderate yet reasonable values for the mantle parameters. To test the sensitivity of our models to the properties of the core, we scan across four different parameters: the abundance of sulfur and potassium in the core, the thermal conductivity of the core, and the present-day heat flux at the CMB.

As with other planets, the Moon's core is expected to be an alloy of iron and light elements, such as sulfur (e.g., Steenstra et al. 2016). Properties of the FeS system are relatively well known (e.g., Fei et al. 1997, 2000, Chudinovskikh & Boehler 2007, Morard et al. 2007, 2008, Stewart et al. 2007, Chen et al. 2008, Buono & Walker 2011, Pommier 2018) and concentrations of sulfur in the lunar core are likely <6–8 wt% based on interpretations of seismic data (e.g., Weber et al. 2011) and models of the lunar core (e.g., Scheinberg et al. 2015, Laneuville et al. 2014). We vary the sulfur abundance, [S], in the bulk core from 1–9 wt% in increments of 0.5 wt%.

Potassium is a potential heat source in planetary cores and soluble in iron alloys at planetary conditions (Murthy et al. 2003, Lee et al., 2004). However, the potassium content of the lunar core remains uncertain. Based on previous studies (e.g., Laneuville et al. 2014, Scheinberg et al. 2015), we test a lower limit of 0 ppm, which assumes a complete lack of radiogenic heating in the lunar core. Although the lower pressures and temperatures in the lunar interior might lead to lower amounts of potassium in the lunar core (e.g., Steenstra et al. 2018), we use plausible concentrations of potassium in Earth's core as an upper limit (e.g., Hirose et al. 2013). In our models, we assume that potassium is incompatible in the inner core, meaning that the outer core becomes enriched in potassium as the inner core grows. We vary the bulk potassium abundance, [K], from 0–50 ppm in increments of 25 ppm.

The thermal conductivity, k_C, of iron alloys defines the adiabatic heat flux of the core. We assume that the maximum plausible value of k_C is ~50 W m^{-1} K^{-1}, cited from thermal conductivity experiments on Fe-FeS alloys in the lunar pressure and temperature range (e.g., Pommier 2018). Small amounts of impurities, such as sulfur, can cause a large reduction in the thermal conductivity. We investigate k_C and [S] independently in our models to isolate the effects of each parameter, but they are coupled in reality. A minimum value of 10 W m^{-1} K^{-1} is selected to represent relatively large impurities of sulfur (e.g., Pommier 2018). Other proposed compositions for the lunar core,

such as Fe-Si alloys, have thermal conductivities that are intermediate between these upper and lower bounds (Berrada et al. 2020). Overall, we vary k_C from 10–50 W m^{-1} K^{-1} in increments of 10 W m^{-1} K^{-1}.

The present-day heat flux at the CMB is highly uncertain and may have been susceptible to higher heat fluxes out of the lower mantle from the enrichment of water and other incompatible elements during solidification of the lunar magma ocean (e.g., Elkins-Tanton & Grove 2011, Khan et al. 2014, Evans et al. 2014, Weiss & Tikoo 2014, Dygert et al. 2017, Greenwood et al. 2018). To monitor how the core's temperature evolves given a certain heat flow, we test a range of values using thermal evolution models as a guide (e.g., Laneuville et al. 2014). After the BMO solidifies, we assume that Q_{CMB} decreases linearly from the final BMO simulation output (~0.90–3.70 GW) to a heat flux value specified at present. We therefore vary the present-day heat flow, Q_C, from 0–2 GW in increments of 1 GW. While the lower limit of 0 GW may represent an extreme scenario, we want to explore a full range of modeling possibilities to account for multiple scenarios for the lunar solid mantle. Furthermore, 1-D models for small planetary bodies typically indicate that the heat flux varies slightly during most of the core's evolution (e.g., Laneuville et al. 2014). We find that model outputs from simulations with a Q_{CMB} equal to the final BMO simulation output are similar to those from models where the Q_{CMB} slightly decreases.

Astute readers will realize that our modeling approach makes the cooling rate of the core seem artificially smooth over time after the BMO solidifies. While the BMO exists, we use Q_{CMB} from the 3-D solid mantle models of Scheinberg et al. (2018), which contain realistic time-variability and fluctuations. Once the BMO has presumably solidified, our parameterized model is effectively 1-D and uses a simplified approach for Q_{CMB} to capture the average field strength and lifetime of the core dynamo. In reality, some smaller-scale temporal variations in Q_{CMB} should be expected and the very last time step is not necessarily representative of the end of the time series.

We ran a total of ~800 simulations to test the sensitivity of the core model to [S], [K], k_C, and Q_C using BMO model outputs from Scheinberg et al. (2018) as boundary conditions.

3. RESULTS

3.1. Our Nominal Model for the Evolution of the Core

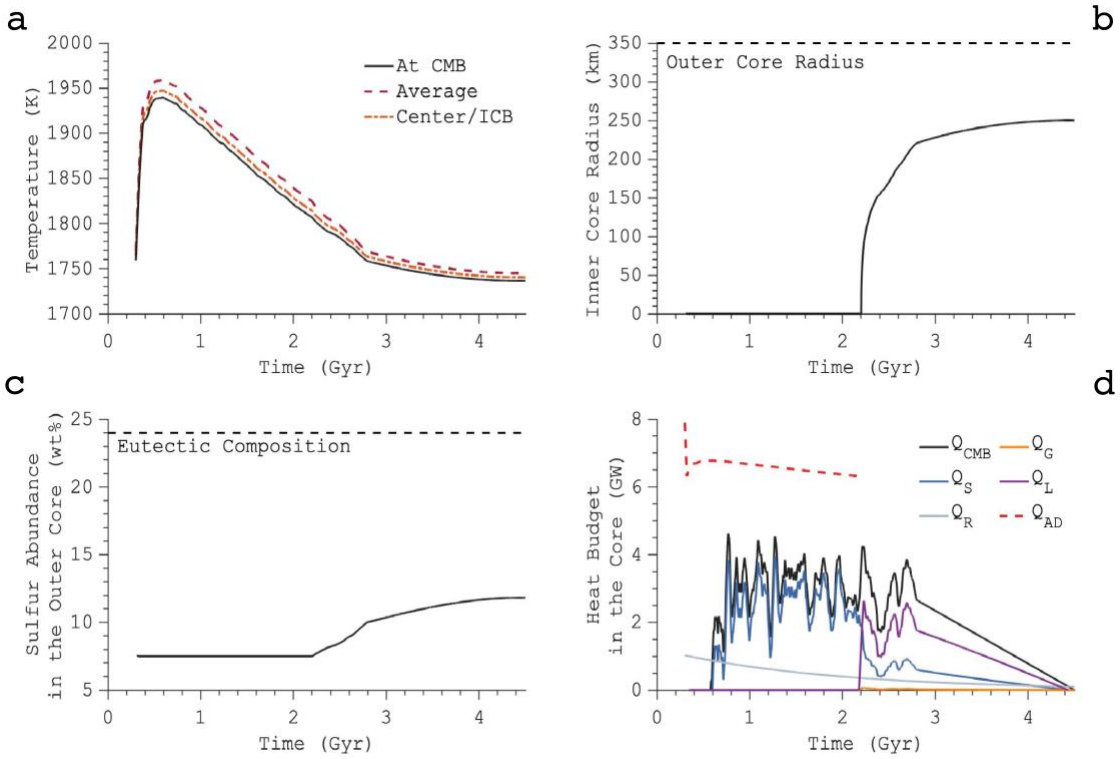

Figure 2: Results of the nominal core model with k_C=40 W m^{-1} K^{-1}, Q_C = 0 GW, [S]=7.5 wt%, and [K] = 25 ppm coupled to the nominal BMO model (V19K50p54). All models began at 4.2 billion years before the present day. (a) Temperature at the core-mantle boundary (CMB), at the center of the core or near the inner core boundary (ICB), and the average temperature of the core. (b) Inner core radius with respect to time. (c) Sulfur abundance in the outer core with respect to time. (d) Heat budget given by latent heat, Q_L, radiogenic heating, Q_R, gravitational energy Q_G, adiabatic heat flow in the core, Q_{AD}, heat flow across the core-mantle boundary, Q_{CMB}, and secular cooling, Q_S.

Our nominal values for the core parameters are [S] = 7.5 wt%, [K] = 25 ppm, k_C = 40 W m^{-1} K^{-1}, and Q_C = 0 GW for the V19K50p54 BMO boundary condition (Table 1). Figure 2 details the outputs of our nominal model for the core coupled to the nominal BMO model (i.e., V19K50p54). The temperature at the CMB begins at ~1760 K and quickly spikes to ~1940 K due to radiogenic heating in the BMO (Fig. 2a). The BMO then begins solidifying as radiogenic heating declines over time, followed by the core cooling in tandem with the BMO. Once the BMO solidifies, an inner core forms at ~2.2 Gyr as relatively pure iron crystallizes from the inside out (Fig. 2b), expelling sulfur into the outer core (Fig. 2c). Our models assume that the lunar core always contains sub-eutectic amounts of sulfur. We verified that this assumption is consistent with our results, which track the sulfur content of the outer core over time

(e.g., Figure 2c). The liquidus temperature of the outer core is lowered as it is progressively enriched in sulfur. The result is a molten outer core and a growing inner core. The heat flow is always less than that transported by thermal conduction along the core adiabat, Q_{AD}. After the inner core nucleates, most extracted heat from the core arises from the release of Q_G and Q_L (Fig. 2d). The release of Q_G is nonzero, but small compared to Q_L. Following the release of Q_G and Q_L, there is a reduction in the core cooling rate due to these heat sources acting as a buffer to secular cooling. We note that the Q_{CMB} is much lower than the heat flow across the upper boundary of the BMO (Q_B = ~100 GW at 2.6 Ga) in Scheinberg et al. (2018) because Q_B includes radiogenic heating in the BMO and the heat associated with cooling the BMO itself.

Abundant sulfur influences the core's ability to drive a magnetic field by lowering its solidus temperature and controlling the onset of inner core crystallization (discussed further in section 3.2.1). The nominal model produces an inner core radius of 250 km at present day (Fig. 2b) and is consistent with core radii derived from calculated models of lunar gravity data (Williams et al. 2014) and reanalyzed Apollo seismic data (Weber et al. 2011).

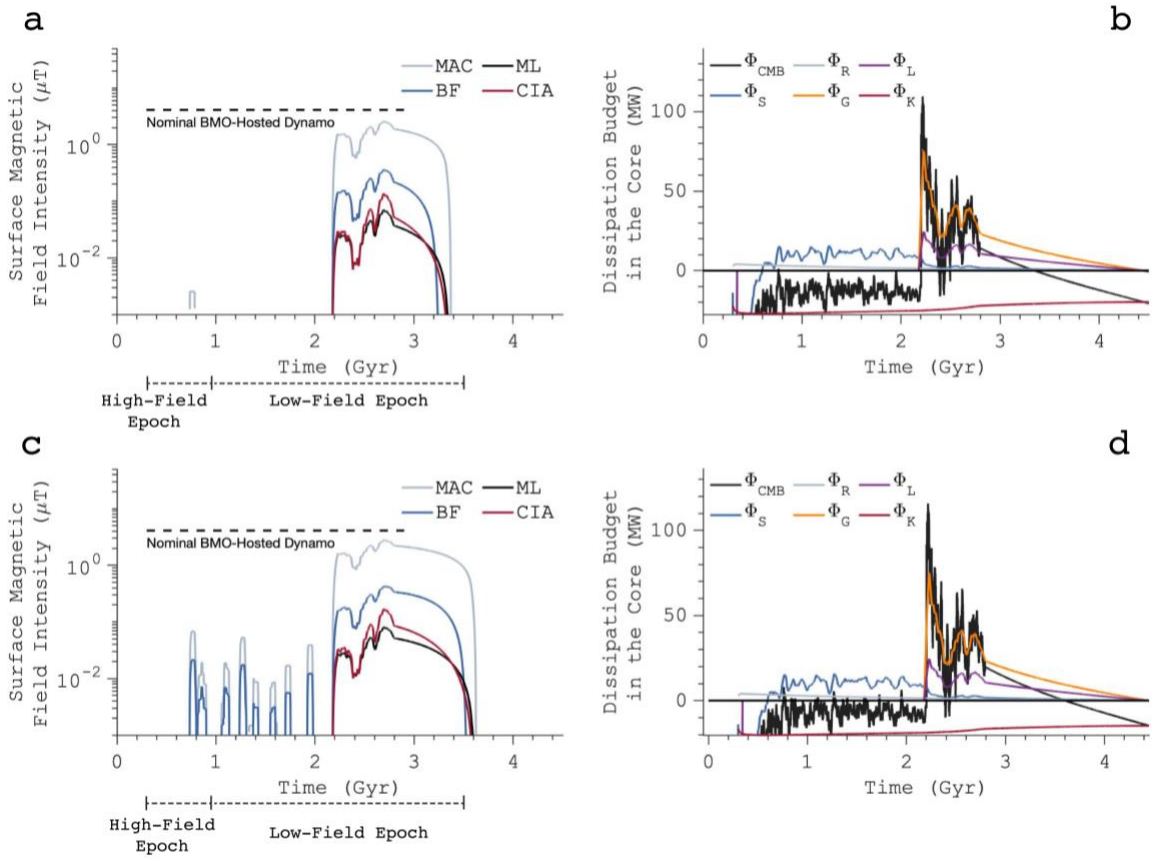

Figure 3: a) Surface field intensities of the nominal core model where core convection is driven by inner core growth relatively late in the Moon's history. The buoyancy flux (BF), mixing length (ML), Coriolis, inertial, gravitational (Archimedes) (CIA), and Magneto-Archimedes-Coriolis (MAC) scaling laws are used to estimate surface field intensities of the dipole component. Surface field intensities are compared to the nominal BMO magnetic field intensity assuming the ML scaling law. (b) The dissipation budget of the nominal core model includes the entropy sink associated with thermal conductivity, Φ_K, the dissipation associated with secular cooling, Φ_S, latent heat, Φ_L, gravitational energy, Φ_G, radiogenic heating, Φ_R, and the dissipation available for a dynamo, Φ_{CMB}. (c) If k_C is lowered to 30 W m^{-1} K^{-1}, purely thermal convection occurs intermittently between ~0.7 and 2 Gyr. Those resultant surface fields are several times weaker than the BMO-hosted field. (d) Dissipation budget associated with a lower k_C of 30 W m^{-1} K^{-1}.

The lunar BMO suppresses convection in the core by lowering its cooling rate. The core produces a dynamo that begins near the cessation of the nominal BMO-hosted dynamo and ends ~1 Ga, consistent with the lower estimate on the cessation of the lunar dynamo derived from radiometric dating of Apollo 15 samples (e.g., Mighani et al. 2020) (Fig. 3a). The relatively weak surface magnetic field strength of $\lesssim$ 2.55 μT is also consistent with paleomagnetic data and intensities from previous models of the lunar core dynamo (e.g., Laneuville et al. 2014, Tikoo et al. 2014, Tikoo et al. 2017, Evans et al. 2018, Mighani et al. 2020).

We next consider different BMO conditions for our core model. Table 1 presents the nominal core input parameters for each BMO boundary condition used in this study. BMOs with a smaller fraction of KREEP that remained near the surface (i.e., V19K25p54 and V18K00p100 in Table 1) have greater initial thicknesses and tend to require lower sulfur abundances (6.5–7 wt%) in the bulk core to initiate dynamo action during the observed timing of the low-intensity epoch. Because a BMO with a greater thickness will have a longer lifetime (e.g., Scheinberg et al. 2018), the core will begin crystallizing at a later time when the BMO eventually solidifies. Conversely, models with shallower BMOs (i.e., 301 km) mostly require higher sulfur abundances in the core (7–8.5 wt%) to achieve a core dynamo during the same period. BMO boundary conditions with greater lifetimes additionally suppress inner core growth for longer periods, resulting in smaller inner core radii at present day. Furthermore, models that contain shallower BMOs match the estimated timing of the lunar dynamo if balanced by less radiogenic heating in the core (i.e., $\leq$ 25 ppm of potassium). In general, BMO boundary conditions typically require the core to have a higher thermal conductivity (i.e., $\geq$ 30 W m^{-1} K^{-1}) to match the estimated timing of the lunar dynamo.

511

Nominal Core Model Inputs						
BMO Boundary Condition	V19K50p54	V19K50p36	V19K50p27	V19K25p54	V18.5K50p54	V18K00p100
BMO lifetime[1] (Gyr)	2.6	2.0	1.6	2.9	1.2	2.1
BMO thickness[1] (km)	301	301	301	383	301	450
[S] (wt%)	7.5	7.0	8.5	7.0	8.5	6.5
[K] (ppm)	25	0	0	50	0	50
Q_C (GW)	0	0	0	0	0	0
k_C ($W\ m^{-1}\ K^{-1}$)	40	10	30	40	30	30

Table 1: Nominal core parameters for each BMO boundary condition used in this study. [1]Values from Scheinberg et al. (2018), Table 1.

512
513
514

515

Nominal Core Model Outputs

BMO Boundary Condition	V19K50p54	V19K50p36	V19K50p27	V19K25p54	V18.5K50p54	V18K00p100
Present-day inner core radius (km)	250	257	231	226	262	241
Compositional convection B_{max} (μT)	0.07 (ML) 0.13 (CIA) 0.36 (BF) 2.55 (MAC)	0.16 0.45 0.77 4.0	0.05 0.09 0.27 2.27	0.03 0.04 0.20 1.7	0.07 0.13 0.40 2.6	0.04 0.08 0.28 2.0
Thermal convection B_{max} (μT)	3×10^{-6}(ML) 3×10^{-7}(CIA) 0.001(BF) 0.003 (MAC)	0.001 3×10^{-4} 0.08 0.30	0.002 0.001 0.07 0.31	3×10^{-4} 9.3×10^{-5} 0.02 0.08	0.001 2×10^{-4} 0.06 0.23	0.002 0.001 0.06 0.28
Combined B_{max} (μT)	0.07 (ML) 0.13 (CIA) 0.36 (BF) 2.55 (MAC)	0.16 0.45 0.85 4.3	0.052 0.091 0.34 2.58	0.03 0.04 0.22 1.78	0.071 0.13 0.46 2.83	0.042 0.081 0.34 2.28
Peak Local Rossby Number	0.02 (CIA) 0.003 (ML) 3×10^{-4} (MAC)	0.03 0.004 4×10^{-4}	0.02 0.003 2×10^{-4}	0.02 0.003 2×10^{-4}	0.02 0.003 2×10^{-4}	0.03 0.003 3×10^{-4}
Compositional convection duration (Gyr)	1.14(ML) 1.14(CIA) 1.06(BF) 1.12(MAC)	1.83 1.75 1.75 1.89	1.90 1.86 1.78 1.95	0.66 0.66 0.58 0.71	2.23 2.23 2.22 2.33	1.42 1.42 1.34 1.49
Thermal convection duration (Gyr)	0.05(ML) 0.05(CIA) 0.05(BF) 0.05(MAC)	0.87 0.87 0.87 0.87	0.08 0.08 0.08 0.08	0.12 0.12 0.12 0.12	0.85 0.85 0.85 0.85	1.65 1.65 1.65 1.65
Lifetime of core-hosted dynamo (Gyr)	1.19(ML) 1.19(CIA) 1.11(BF) 1.17(MAC)	2.70 2.62 2.62 2.76	1.98 1.94 1.86 2.03	0.78 0.78 0.7 0.83	3.08 3.08 3.07 3.18	3.07 3.07 2.99 3.14

Table 2: Compositional and thermal convection in the core sustains low intensity magnetic fields following the cessation of a BMO-hosted dynamo. B_{max} is the peak magnetic field intensity at the surface according to the ML, CIA, BF, and MAC magnetic field scaling laws, respectively, assuming that the mantle is electrically insulating. Thermal convection B_{max} corresponds to the ML, CIA, BF and MAC scalings, respectively. The combined B_{max} is the sum of surface fields generation from thermal and compositional convection. The peak local Rossby number corresponds to the CIA, ML, and MAC scaling laws, respectively. The thermal convection duration corresponds to the ML, CIA, BF, and MAC scalings, respectively.

516

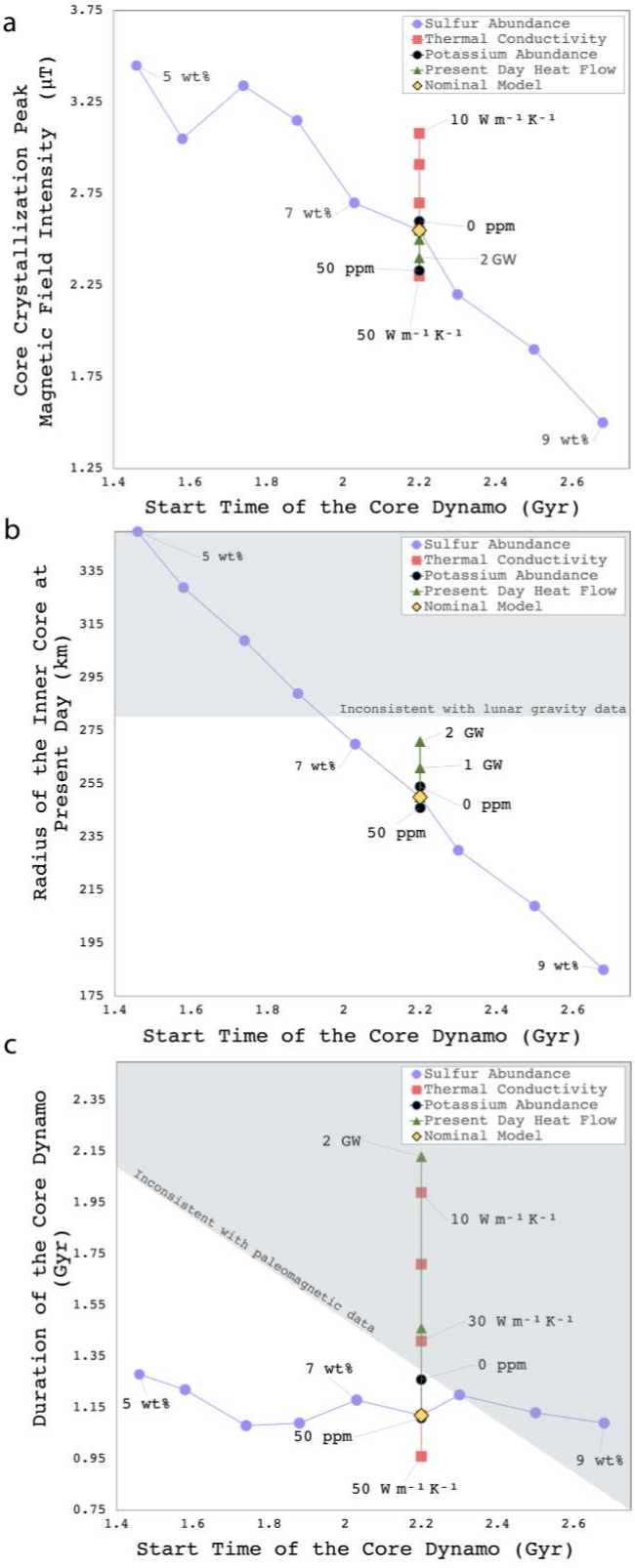

Figure 4: The sensitivities of the nominal core model to core parameters k_c, [K], [S], and Q_c for the nominal V19K50p54 BMO model. (a) The surface magnetic field intensity is most sensitive to k_c and [S] and less sensitive to [K] and Q_c. (b) Our choice of [S] controls the predicted timing of inner core growth and thus, a compositionally-driven core dynamo. The shaded region represents inner core radii that are probably inconsistent with lunar gravity data (e.g., Williams et al. 2014). (c) The duration of the dynamo is predicted to increase with increasing Q_c and decreasing k_c. High [S] tends to delay the onset of inner core crystallization and result in a shorter field duration. The shaded region represents durations that are likely inconsistent with constraints on the end of the lunar dynamo (e.g., Mighani et al. 2020). The magnetic field intensity and the duration of the core dynamo are given by the MAC scaling law.

3.2. Sensitivity Tests

3.2.1. Influence of Sulfur in the Core

An inverse relationship exists between the sulfur content and the solidus temperature of the core. As the sulfur content increases, the solidus temperature of the Fe–S system decreases, delaying core solidification until lower temperatures are reached. Therefore, the timing of inner core growth, and thus, the start time of compositional convection in

our models depends on the sulfur content of the bulk core (Fig. 4a). The sulfur concentration is viable when the end of the core-hosted dynamo matches the lower estimate on the cessation of the lunar dynamo at ~1 Gyr (e.g., Mighani et al. 2020). Initial sulfur abundances of 1–6.5 wt% result in inner core nucleation at higher temperatures, causing the core to solidify rapidly early in its history (Fig. 4b). Sulfur abundances from 7–8.5 wt% result in the inner core nucleating near the cessation of the BMO-hosted dynamo. Increasing the bulk sulfur content to >8.5 wt% further delays inner core growth and generally results in temporal gaps between the BMO-hosted and core-hosted dynamo, a complete lack of core dynamo action, or contradictions with timing estimates derived from paleomagnetic data (Fig. 4c). However, if the BMO model assumes a lower solid mantle viscosity (i.e., V18.5K50p54), then convective heat transfer is more efficient and results in shorter BMO lifetimes (Scheinberg et al. 2018). As a result, the inner core begins crystallizing earlier and a bulk sulfur content of up to 12 wt% can produce results consistent with the lower estimate on the cessation of the lunar dynamo (e.g., Mighani et al. 2020). The trends outlined in Fig. 4 that arise from variations in k_c, [K], [S], and Q_c continue under all other BMO boundary conditions.

3.2.2. Influence of the Core's Heat Budget and Thermal Conductivity

The duration and intensity of the core dynamo are also sensitive to k_c, Q_c, and [K] (Figure 4). A potassium abundance of 50 ppm in the core contributes thermal energy to the dynamo but suppresses growth of the inner core, which can decrease the predicted intensity of the magnetic field overall. Decreasing [K] has a minimal effect on the field intensity because radiogenic heating is nearly equivalent to secular cooling in the dissipation budget. In contrast, increasing the total heat flow to 1–2 GW increases the duration and strength of the core-hosted dynamo, unless a low sulfur abundance leads to rapid core solidification. Furthermore, the duration and intensity of the field generally increases with decreasing thermal conductivity values. We find that purely thermal convection typically occurs before the onset of inner core crystallization if the thermal conductivity is low (i.e., 10–30 W m^{-1} K^{-1} as in Fig. 3c). As thermal conductivity decreases, the super-adiabatic heat flow increases, leading to a stronger, more long-lived dynamo. Thermal convection-driven dynamos typically occur simultaneously with BMO-hosted dynamos as the core is still hot and fully

molten. Compared to the abundance of sulfur in the bulk core, our simulations reveal that small variations in parameters such as k_C, Q_C, and [K] play an overall negligible role in the onset of a compositionally-driven dynamo, whereas a thermal convection-driven dynamo is largely dictated by k_C.

3.2.3. Strength and Timing of the Core Dynamo

Depending on the BMO boundary condition, inner core crystallization can produce fields ~0.7–2.3 Gyr in duration, with peak magnetic fields of 0.16, 0.45, 0.77, and 4 μT, for the ML, CIA, BF, and MAC scaling laws respectively (Table 2). A general issue arises in the case of the CIA, ML, and BF scalings laws in which the strengths are not sufficiently strong enough to reproduce the first period of decline to ~4–7 μT by 3.19 Ga (e.g., Strauss et al. 2021) or the second period of decline to ~5 ± 2 μT by ~1–2 Ga (e.g., Tikoo et al. 2017, Mighani et al. 2020). However, intensities ranging from ~1.7–4 μT can be achieved under all BMO boundary conditions if the MAC scaling law is assumed. In particular, an intensity of 4 μT is achieved if the BMO boundary condition contains a lower fraction of radioactive material concentrated in the BMO (i.e., V19K50p36). However, this magnetic field weakens to a maximum of 4 μT ~2 Gyr after accretion, which is ~0.7 Gyr later than what is observed in the lunar paleomagnetic record (Strauss et al. 2021).

Surface magnetic fields are weaker if they are driven by thermal convection rather than by inner core crystallization. The peak surface magnetic field driven by thermal convection in the nominal core model is 3×10^{-6}, 3×10^{-7}, 0.001, and 0.003 μT for the ML, CIA, BF, and MAC scaling laws, respectively (Table 2). For all BMO boundary conditions, thermal convection in the core is initiated ~3.7 Gyr ago (albeit briefly in some models; e.g., Fig. 3a). Furthermore, depending on the BMO boundary condition, thermal convection can persist intermittently for up to ~1.7 Gyr, resulting in an overlap with the BMO-hosted field (e.g., Fig. 3c). Thermal convection produces intensities that are consistent with previous modeled estimates of the core (e.g., Laneuville et al. 2014, Evans et al. 2018, Scheinberg et al. 2015), but inconsistent with paleomagnetic analyses constraining the initial and final decline of the lunar dynamo (e.g., Tikoo et al. 2017, Mighani et al. 2020, Strauss et al. 2021). Furthermore, these results are consistent with a low-intensity epoch that persisted from ~1.9–0.8 Ga (e.g., Mighani et al. 2020, Tikoo et al. 2017, Tikoo et al. 2014, Strauss et al. 2021).

An uneven heat flow across the CMB may make the magnetic field intermittent because dynamos can be sensitive to slight variations in heat flow (Scheinberg et al. 2015). As an artifact of our modeling approach, early magnetic fields produced via thermal convection are discontinuous due to fluctuations in the Q_{CMB} from mantle dynamics. In some cases, thermal convection generates fields that are predicted to drop to zero multiple times before rising again from inner core crystallization. The duration of these gaps in the magnetic field are much longer than the magnetic diffusion time (Appendix C). Using the nominal models but with core conductivity lowered to k_C = 30 W m^{-1} K^{-1} as an example case (i.e., Fig 3c), gaps in thermal convection on average last ~140 Myr, whereas the magnetic diffusion time is only a few hundred years. Alternatively, dynamos induced by thermal convection can transition directly into those induced by inner core crystallization, compounding the resultant fields.

3.3. Local Rossby Number

In order to make initial predictions for the magnetic field morphologies in our models, we estimate the local Rossby number as a proxy for whether the core dynamos would be dipole-dominated or multipolar, as for example has been done previously for Ganymede's dynamo (Rückriemen et al. 2015). The CIA scaling law predicts higher values of the local Rossby number (Ro_l ~ 10^{-2}) relative to the ML (Ro_l ~ 10^{-3}) and MAC (Ro_l ~ 10^{-4}) scaling laws since inertia plays a larger role in the force balance (Christensen & Aubert 2006). However, for the nominal core model, all scaling laws predict that the local Rossby number is below the threshold value of ~0.1 throughout the lifetime of the core dynamo, suggesting a prevailing dipole-dominated magnetic field (Table 2 and Figure 5).

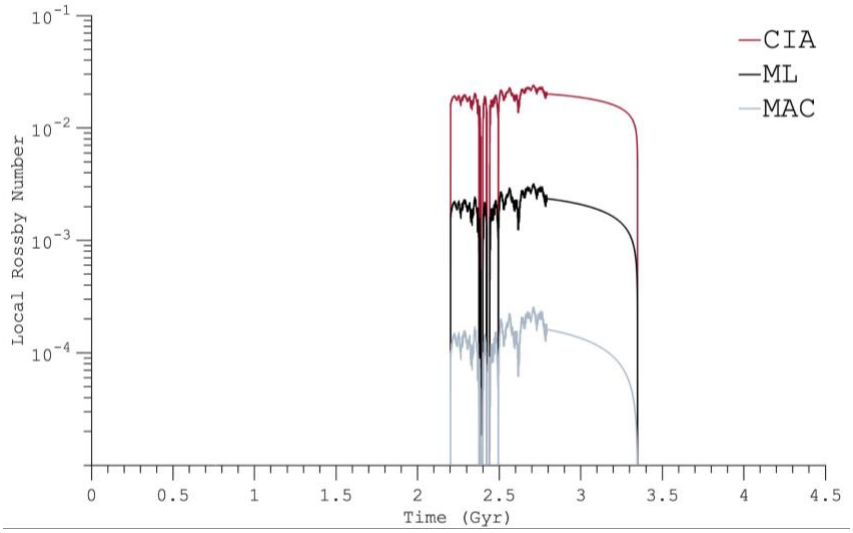

Figure 5: Predictions of the local Rossby number for the nominal core model estimated from CIA, ML, and MAC scaling laws.

4. DISCUSSION

In this study, we demonstrated that a BMO dynamo could naturally dovetail with a core dynamo. Future studies should further explore this hypothesis by addressing the following important issues.

4.1. Other Modes of Crystallization in the Core

Future studies could model more complex modes of crystallization in the lunar core. To recap, we made two relevant assumptions. First, we assumed that the core always contains sub-eutectic amounts of sulfur, which most of our models indeed predict (section 3.3). Second, we assumed that the core solidifies from the center outwards. We set the liquidus temperature to increase faster than the adiabatic temperature with pressure (e.g., with gradients of 30 K/GPa versus ~23–25 K/GPa, respectively).

Future studies could relax these two assumptions, which would produce more complicated behavior in models (e.g., Hauck et al. 2006). First, FeS rather than Fe could crystallize from the outer core as it cooled if the sulfur content were super-eutectic. Being sulfur-rich compared to the residual liquid, solid FeS would float to the top of the liquid rather than sink to form an inner core like solid Fe. Second, solidification could occur at the top or middle of the outer core, rather than at its bottom. For example, "iron snow" could occur in metallic cores if the liquidus crosses the adiabat above the base of the outer core. This process could help drive a dynamo as the solidified iron sinks and remelts in the warmer fluid below,

leading to compositional convection (e.g., Williams 2009, Breuer et al. 2015). Whether the Moon's core entered an FeS crystallization or Fe snow regime at any time remains an ongoing question.

Scientists might make more realistic models of the thermal evolution of sulfur-rich cores if they include these processes. Such models require detailed phase diagrams for the Fe-FeS system. The neglect of Fe snow and FeS crystallization in our models does not change our takeaway message, however, that the presence of a basal magma ocean overlying the core may influence the timing and intensity of the core dynamo. Our models may interface with future, more detailed descriptions of Fe snow and FeS in the core.

4.2. Morphology of the Lunar Dynamo

The geometry and paleo-orientation of the Moon's magnetic field remains largely uncertain. Estimates of paleoinclinations from five Apollo samples suggest the existence of a dipolar field and a paleopole located at ~75°N between 3.8 and 3.3 billion years ago (e.g., Cournède et al. 2012). These findings are possibly best explained with a paleofield geometry close to the present-day rotation axis of the Moon. Assumptions of the paleopole were made based on the location of Apollo samples: samples collected from the northern hemisphere were given a positive declination while samples collected from the southern hemisphere were given a negative declination. However, the sign of the inclination remains largely unknown and more data is required to confirm interpretations made from lunar samples. Studies of Apollo 17 mare basalts estimated an inclination of ~34° based on the layering of its parent boulder (Nichols et al. 2021). This inclination is consistent with, but does not require, a dipole in the center of the Moon aligned along its rotation axis.

Conversely, Olson & Christensen (2006) hypothesized that the Moon's magnetic field may have been multipolar rather than dipole-dominated. The critical difference between our studies is the amplitude of buoyancy flux in the core. Their study assumed that the average buoyancy flux associated with convection in the lunar core was 0.3 times the terrestrial value. That is, F_{Moon} = 0.3 F_{Earth}, where $F = \alpha g Q / (\rho C_p)$ with thermal expansivity α, gravitational acceleration g, convective heat flux Q, density ρ, and specific heat capacity C_p. This assumption was based on the idea that tidal dissipation could add several TW of power to the ancient lunar core (e.g., Williams et al. 2001). This larger heat flow leads to larger estimates of the local Rossby number (e.g., Ro_l ~ 2), which would shift the lunar dynamo into a multipolar regime.

In contrast, our models do not include tidal heating in the lunar core. So, the total power available for convection is only several GW in our models, as shown in Figure 2d.

It is also possible that the directional magnetization of lunar rocks does not record a long-term orientation of the lunar magnetic field since differential rotations between the mantle and core would cause a core dipole field to drift across the lunar surface (e.g., Ćuk et al. 2019). Relative motions of the core and mantle or misalignment between the lunar dynamo and spin axis may further explain the great variability in the inferred orientation of the lunar dynamo from proposed paleopole locations (e.g., Oliveira & Wieczorek 2017, Nayak et al., 2017). Future missions sampling the lunar bedrock along varying latitudes will allow for more precise geometric determinations of the Moon's magnetic field.

4.3. Electromagnetic Core – Mantle Coupling

The effects of an electrically conducting lower mantle on the core dynamo is not considered in our study. This limitation is significant for several reasons. First, as noted in Section 2.3, the relatively large conductivity of the BMO, especially when it is fully liquid, will likely cause our estimates of surface magnetic field strengths to be artificially small compared to if this conductivity were taken into account. Our estimates for the core field strength assume that the entire mantle, including the BMO, is electrically insulating such that the core-generated magnetic field becomes a potential field that diffuses upward through the mantle. Given the anticipated higher conductivity of metalliferous silicate melts compared to solid mantle rocks (e.g., Scheinberg et al. 2018), the top of the dynamo region may effectively be the top of the BMO, rather than the top of the core, even if the BMO is subcritical for dynamo action.

Second, fluid flows within the BMO may also modulate the core field itself (e.g., Gómez-Pérez et al. 2010). Conversely, if the BMO fluid is stably-stratified, its presence may still filter out small-scale components of the core field that rapidly vary via the magnetic skin effect (e.g., Christensen 2006). Third, the BMO may have resulted in larger magnetic coupling between the core-mantle in the past, relevant to studies of the Moon's rotational dynamics over time (e.g., Dumberry & Wieczorek 2016). Further work, such as numerical dynamo modeling, is needed to better understand the full degree of coupling between the BMO and core of the Moon.

4.4. Thermal Stratification in the Core

The effects of thermal stratification in the lunar core are not considered in this study. The inclusion of thermal stratification can have several effects on the heat flux at the CMB. Studies of Mercury's core (e.g., Knibbe and Westrenen 2018, Knibbe and van Hoolst 2021) found that thermal stratification can lead to an increased inner core size, higher temperatures, and a larger heat flux at the CMB, which together results in an early start to the magnetic field. Subsequent heat released upon core solidification would enable slow core growth and an active magnetic field until present day. Future work could apply these models of Mercury to the Moon.

4.5. The Early Evolution of the Moon

Thermal stratification is probably inevitable at present day, but could also exist early in the Moon's history. In this study, we assumed that the core was initially fully molten and had an adiabatic temperature gradient. If radiogenic heating in the BMO ever made the bottom of the BMO hotter than the top of the core, then heat would move from the BMO into the core, which would cause thermal stratification at the top of the core that may delay the start of a core-hosted dynamo. However, the Moon could have formed with "superheat" (such that the core was initially hotter than the BMO)(e.g., Evans et al. 2018), in which case the core could deliver heat to the BMO even while the BMO heats up radiologically. Neither our study nor Scheinberg et al. (2018) modeled these two, countervailing possibilities in detail. Further work is thus needed to better understand the formation and early evolution of the Moon.

5. CONCLUSIONS

Our model for the coupled evolution of a basal magma ocean and the core places estimates on the abundance of sulfur in the core (i.e., 6.5–8.5 wt% in Table 1) and can explain the timing and relative intensity of the lunar magnetic field consistent with other models of the lunar core (e.g., Laneuville et al. 2014, Evans et al. 2018, Scheinberg et al. 2015). The basal magma ocean does not need to be electrically conductive to explain the results presented here, even if it was required to explain the results of

Scheinberg et al. (2018). While that may mean the early, intense lunar dynamo remains unexplained, we find that the predicted timing of the lunar dynamo in our models is most consistent with observational constraints of the long-lived low-intensity period when moderate abundances of sulfur and potassium are assumed in the core, the core's thermal conductivity is high, and if the present-day CMB heat flow is assumed to be low (or even zero). Excessively high values of Q_{CMB} at present day (i.e., 1–2 GW) tends to increase the duration of the magnetic fields longer than is consistent with timing constraints on the end of the lunar dynamo (e.g., Mighani et al. 2020). Modeled intensities are most consistent with paleomagnetic analyses constraining the initial and final decline of the lunar dynamo (e.g., Tikoo et al. 2017, Mighani et al. 2020, Strauss et al. 2021) when the BMO boundary condition is assumed to have less radiogenic heating concentrated in the BMO or when the MAC scaling is assumed. Other scaling laws (i.e., CIA, ML, and BF) predict that magnetic field intensities would be ~1–2 orders of magnitude weaker at the surface than inferred from paleomagnetic data (although recall that our intensities may be higher if electrical conductivity of the BMO is taken into account).

Thermal convection can briefly exist with the BMO, but is generally short-lived (Fig 3a) or intermittent (Fig 3c), generating magnetic field intensities of up to ~0.3 μT that persist for ≲1.7 Gyr (Table 2). Near cessation of the lunar BMO dynamo, heat flows are too low for purely thermal convection and later dynamo action requires inner core crystallization. Magnetic fields generated from the onset of inner core crystallization can reach intensities of up to ~4 μT and can persist for ≲2.3 Gyr (Table 2). Temporal gaps may arise between dynamos powered by different types of energy in the core (i.e., thermal vs. compositional), which are neither confirmed nor excluded by extant data. Temporal gaps in the magnetic field can lead to complications in interpretations of the paleomagnetic record and may indicate that a portion of Apollo samples with null paleointensities (e.g., Tarduno et al. 2021) may not result from poor magnetic recording properties.

Estimates of the core sulfur abundance from our model can further translate into predictions of the radius of the inner core. These predictions can be verified with future missions, such as the Farside Seismic Suite (e.g., Panning et al. 2021), which will provide new constraints on the internal structure of the Moon, and the Lunar Geophysical Network (e.g., Weber et al. 2021), which aims to understand the size, state, and composition of the lunar core and the chemical and physical stratification of the mantle.

Together, these findings will help discriminate between hypotheses that seek to explain the high–low intensity epoch. Research on the Moon's magnetic history should remain fruitful for decades.

6. ACKNOWLEDGMENTS

This material is based upon work supported by the National Science Foundation Graduate Research Fellowship under Grant No. 026257-001. We thank Aaron Scheinberg for providing the complete outputs of published simulations.

7. REFERENCES

Berrada, M., Secco, R. A., Yong, W., & Littleton, J. A. H. (2020). Electrical Resistivity Measurements of Fe-Si With Implications for the Early Lunar Dynamo. *Journal of Geophysical Research: Planets*, *125*(7), 1–15. https://doi.org/10.1029/2020JE006380

Bland, M. T., Showman, A. P., & Tobie, G. (2008). The production of Ganymede's magnetic field. *Icarus*, *198*(2), 384–399. https://doi.org/10.1016/j.icarus.2008.07.011

Blaske, C. H., & O'Rourke, J. G. (2021). Energetic Requirements for Dynamos in the Metallic Cores of Super-Earth and Super-Venus Exoplanets. *Journal of Geophysical Research: Planets*, *126*(7), 1–19. https://doi.org/10.1029/2020JE006739

Breuer, D., Rueckriemen, T., & Spohn, T. (2015). Iron snow, crystal floats, and inner-core growth: modes of core solidification and implications for dynamos in terrestrial planets and moons. Progress in Earth and Planetary Science, 2(1). https://doi.org/10.1186/s40645-015-0069-y

Bullard, E. C. (1949). The magnetic field within the earth. Proceedings of the Royal Society of London. Series A. Mathematical and Physical Sciences, 197(1051), 433–453. https://doi.org/10.1098/rspa.1949.0074

Bullen, K. E. (1954). On the Homogeneity, or Otherwise, of the Earth's Upper Mantle. American Geophysical Union, 33(5). https://doi.org/10.1029/TR035i005p00838.

Buono, A. S., & Walker, D. (2011). The Fe-rich liquidus in the Fe-FeS system from 1bar to 10GPa. *Geochimica et Cosmochimica Acta*, *75*(8), 2072–2087. https://doi.org/10.1016/j.gca.2011.01.030

Cameron, A. G. W. (1973). Abundances of the Elements in the Solar System. Space Science Reviews, 15, 121–146.

Canup, R. M. (2012). Forming a Moon with an Earth-like Composition via a Giant Impact. Science, 338(6110), 1052–1055. https://doi.org/10.1126/science.1226073.

Chen, B., Li, J., & Hauck, S. A. (2008). Non-ideal liquidus curve in the Fe-S system and Mercury's snowing core. *Geophysical Research Letters*, *35*(7), 10-14. https://doi.org/10.1029/2008GL033311

Christensen, U. R. (2006). A deep dynamo generating Mercury's magnetic field. *Nature*, 444(7122), 1056-1058.

Christensen, U. R., & Aubert, J. (2006). Scaling properties of convection-driven dynamos in rotating spherical shells and application to planetary magnetic fields. *Geophysical Journal International*, *166*(1), 97-114. https://doi.org/10.1111/j.1365-246X.2006.03009.x

Christensen, U. R., Holzwarth, V., & Reiners, A. (2009). Energy flux determines magnetic field strength of planets and stars. *Nature*, 457(7226), 167–169. https://doi.org/10.1038/nature07626

Christensen, U. r. (2010). Dynamo scaling laws and applications to the planets. *Space science reviews*, *152*(1), 565-590. https://doi.org/10.1007/s11214-009-9553-2

Chudinovskikh, L., & Boehler, R. (2007). Eutectic melting in the system Fe-S to 44 GPa. *Earth and Planetary Science Letters*, 257(1–2), 97–103. https://doi.org/10.1016/j.epsl.2007.02.024

Cournède, C., Gattacceca, J., & Rochette, P. (2012). Magnetic study of large Apollo samples: Possible evidence for an ancient centered dipolar field on the Moon. *Earth and Planetary Science Letters*, *331–332*, 31–42. https://doi.org/10.1016/j.epsl.2012.03.004

Ćuk, M., Hamilton, D. P., & Stewart, S. T. (2019). Early dynamics of the lunar core. *Journal of Geophysical Research: Planets*, *124*(11), 2917-2928.

Ćuk, M. & Stewart, S. T. (2012). Making the Moon from a Fast-Spinning Earth: A Giant Impact Followed by Resonant Despinning. *Science*, 338(6110), 1047–1052. https://doi.org/ 10.1126/science.1225542

Dasgupta, R., Buono, A., Whelan, G., & Walker, D. (2009). High-pressure melting relations in Fe-C-S systems: Implications for formation, evolution, and structure of metallic cores in planetary bodies. *Geochimica et Cosmochimica Acta*, *73*(21), 6678–6691. https://doi.org/10.1016/j.gca.2009.08.001

Davies, C. J., & Pommier, A. (2018). Iron snow in the Martian core?. *Earth and Planetary Science Letters*, *481*, 189-200. https://doi.org/10.1016/j.epsl.2017.10.026

Dumberry, M., & Wieczorek, M. A. (2016). The forced precession of the Moon's inner core. *Journal of Geophysical Research: Planets*, *121*(7), 1264-1292.

Dwyer, C. A., Stevenson, D. J., & Nimmo, F. (2011). A long-lived lunar dynamo driven by continuous mechanical stirring. *Nature*, *479*(7372), 212–214. https://doi.org/10.1038/nature10564

Dygert, N., Lin, J. F., Marshall, E. W., Kono, Y., & Gardner, J. E. (2017). A Low Viscosity Lunar Magma Ocean Forms a Stratified Anorthitic Flotation Crust

With Mafic Poor and Rich Units. Geophysical Research Letters, 44(22), 11,282-11,291. https://doi.org/10.1002/2017GL075703

Elardo, S. M., Draper, D. S., & Shearer, C. K. (2011). Lunar Magma Ocean crystallization revisited: Bulk composition, early cumulate mineralogy, and the source regions of the highlands Mg-suite. *Geochimica et Cosmochimica Acta*, *75*(11), 3024–3045. https://doi.org/10.1016/j.gca.2011.02.033

Elsasser, W. M. (1950). The Earth's Interior and Geomagnetism. Reviews of Modern Physics, 22(1). https://doi.org/10.1103/RevModPhys.22.1.

Elkins-Tanton, L. T., & Grove, T. L. (2011). Water (hydrogen) in the lunar mantle: Results from petrology and magma ocean modeling. *Earth and Planetary Science Letters*, *307*(1–2), 173–179. https://doi.org/10.1016/j.epsl.2011.04.027

Elkins-Tanton, L. T., Burgess, S., & Yin, Q. Z. (2011). The lunar magma ocean: Reconciling the solidification process with lunar petrology and geochronology. *Earth and Planetary Science Letters*, *304*(3–4), 326–336. https://doi.org/10.1016/j.epsl.2011.02.004

Evans, A. J., Zuber, M. T., Weiss, B. P., & Tikoo, S. M. (2014). A wet, heterogeneous lunar interior: Lower mantle and core dynamo evolution. *Journal of Geophysical Research E: Planets*, *119*(5), 1061–1077. https://doi.org/10.1002/2013JE004494

Evans, A. J., & Tikoo, S. M. (2022). An episodic high-intensity lunar core dynamo. *Nature Astronomy*. https://doi.org/10.1038/s41550-021-01574-y

Evans, A. J., Tikoo, S. M., & Andrews-Hanna, J. C. (2018). The Case Against an Early Lunar Dynamo Powered by Core Convection. *Geophysical Research Letters*, *45*(1), 98–107. https://doi.org/10.1002/2017GL075441

Fei, Y., Bertka, C. M., & Finger, L. W. (1997). High-pressure iron-sulfur compound, Fe3S2, and melting relations in the Fe-FeS system. Science, 275(5306), 1621–1623. https://doi.org/10.1126/science.275.5306.1621

Fei, Y., Li, J., Bertka, C. M., & Prewitt, C. T. (2000). Structure type and bulk modulus of Fe3S, a new iron-sulfur compound. American Mineralogist, 85(11–12), 1830–1833. https://doi.org/10.2138/am-2000-11-1229

Garcia, R. F., Gagnepain-Beyneix, J., Chevrot, S., & Lognonné, P. (2011). Very preliminary reference Moon model. *Physics of the Earth and Planetary Interiors*, *188*(1–2), 96–113. https://doi.org/10.1016/j.pepi.2011.06.015

Glatzmaier, G. A., & Roberts, P. H. (1995). A three-dimensional convective dynamo solution with rotating and finitely conducting inner core and mantle. Physics of the Earth and Planetary Interiors, 91(1–3), 63–75. https://doi.org/10.1016/0031-9201(95)03049-3

Gómez-Pérez, N., Heimpel, M., & Wicht, J. (2010). Effects of a radially varying electrical conductivity on 3D numerical dynamos. *Physics of the Earth and Planetary Interiors*, *181*(1-2), 42-53.

Hamid, S. H., & O'Rourke, J. G. (2022). Modeling of the Lunar Magma Ocean. In: Cudnik B. (eds) Encyclopedia of Lunar Science. Springer, Cham.

Hartmann, William, K., & Davis, D. R. (1975). Satellite-Sized Planetesimals and Lunar Origin. *Icarus*, *24*, 504–515.

Hauck, S. A., Aurnou, J. M., & Dombard, A. J. (2006). Sulfur's impact on core evolution and magnetic field generation on Ganymede. *Journal of Geophysical Research E: Planets*, *111*(9), 1–14. https://doi.org/10.1029/2005JE002557

Hess, P. C., & Parmentier, E. M. (1995). A model for the thermal and chemical evolution of the Moon's interior: implications for the onset of mare volcanism. *Earth and Planetary Science Letters*, *134*(3–4), 501–514. https://doi.org/10.1016/0012-821X(95)00138-3

Hirose, K., Labrosse, S., Herlund, J. (2013). Composition and State of the Core. *Annual Review of Earth and Planetary Sciences*, *41*(1), 657-691. https://doi.org/10.1146/annurev-earth-050212-124007.

Hood, L. L., Mitchell, D. L., Lin, R. P., Acuna, M. H., & Binder, A. B. (1999). Initial measurements of the lunar induced magnetic dipole moment using lunar prospector magnetometer data. *Geophysical Research Letters*, *26*(15), 2327–2330. https://doi.org/10.1029/1999GL900487

Kageyama, A., Sato, T., Watanabe, K., Horiuchi, R., Hayashi, T., Todo, Y., Watanabe, T. H., & Takamaru, H. (1995). Computer simulation of a magnetohydrodynamic dynamo. II. Physics of Plasmas, 2(5), 1421–1431. https://doi.org/10.1063/1.871485

Khan, A., Connolly, J. A. D., Pommier, A., & Noir, J. (2014). Geophysical evidence formelt in the deep lunar interior and implications for lunar evolution. *Journal of Geophysical Research E: Planets*, *119*(10), 2197–2221. https://doi.org/10.1002/2014JE004661

Khan, A., Liebske, C., Rozel, A., Rivoldini, A., Nimmo, F., Connolly, J. A. D., Plesa, A. C., & Giardini, D. (2018). A Geophysical Perspective on the Bulk Composition of Mars. *Journal of Geophysical Research: Planets*, *123*(2), 575–611. https://doi.org/10.1002/2017JE005371

Labrosse, S. (2014). Thermal evolution of the core with a high thermal conductivity. *Physics of the Earth and Planetary Interiors*, *247*, 36–55. https://doi.org/10.1016/j.pepi.2015.02.002

Laneuville, M., Wieczorek, M. A., Breuer, D., Aubert, J., Morard, G., & Rückriemen, T. (2014). A long-lived lunar dynamo powered by core crystallization. *Earth and Planetary Science Letters*, *401*, 251–260. https://doi.org/10.1016/j.epsl.2014.05.057

Le Bars, M., Wieczorek, M. A., Karatekin, A., Cébron, D., & Laneuville, M. (2011). An impact-driven dynamo for the early Moon. *Nature*, *479*(7372), 215–218. https://doi.org/10.1038/nature10565

Lee, K. K. M., Steinle-Neumann, G., & Jeanloz, R. (2004). Ab-initio high-pressure alloying of iron and potassium: Implications for the Earth's core.

Geophysical Research Letters, *31*(11), 1–4. https://doi.org/10.1029/2004GL019839

Meyer, J., & Wisdom, J. (2011). Precession of the lunar core. *Icarus*, *211*(1), 921–924. https://doi.org/10.1016/j.icarus.2010.09.016

Mighani, S., wang, H., Shuster, D. L., Cauê, S. B., Nichols, C. I. O., & Weiss, B. P. (2020). The end of the lunar dynamo. Science Advances, 6, 1–8.

Morard, G., Sanloup, C., Fiquet, G., Mezouar, M., Rey, N., Poloni, R., & Beck, P. (2007). Structure of eutectic Fe-FeS melts to pressures up to 17 GPa: Implications for planetary cores. Earth and Planetary Science Letters, 263(1–2), 128–139. https://doi.org/10.1016/j.epsl.2007.09.009

Morard, G., Andrault, D., Guignot, N., Sanloup, C., Mezouar, M., Petitgirard, S., & Fiquet, G. (2008). In situ determination of Fe-Fe3S phase diagram and liquid structural properties up to 65 GPa. Earth and Planetary Science Letters, 272(3–4), 620–626. https://doi.org/10.1016/j.epsl.2008.05.028

Murthy, V. R., Van Westrenen, W., & Fei, Y. (2003). Experimental evidence that potassium is a substantial radioactive heat source in planetary cores. *Nature*, *423*(6936), 163–165. https://doi.org/10.1038/nature01560

Nakajima, M., & Stevenson, D. J. (2014). Investigation of the dynamol state of the Moon-forming disk: Bridging SPH simulations and hydrostatic models. Icarus, 233, 259–267. https://doi.org/10.1016/j.icarus.2014.01.008

Nayak, M., Hemingway, D., & Garrick-Bethell, I. (2017). Magnetization in the South Pole-Aitken basin: Implications for the lunar dynamo and true polar wander. Icarus, 286, 153–192. https://doi.org/10.1016/j.icarus.2016.09.038

Nemchin, A., Timms, N., Pidgeon, R., Geisler, T., Reddy, S., & Meyer, C. (2009). Timing of crystallization of the lunar magma ocean constrained by the oldest zircon. Nature Geoscience, 2(2), 133–136. https://doi.org/10.1038/ngeo417.

Nichols, C. I. O., Weiss, B. P., Getzin, B. L., Schmitt, H. H., Béguin, A., Rae, A. S. P., & Shah, J. (2021). The palaeoinclination of the ancient lunar magnetic field from an Apollo 17 basalt. *Nature Astronomy*, *5*(12), 1216–1223. https://doi.org/10.1038/s41550-021-01469-y

Nimmo, F. (2015). Energetics of the core, Treatise on Geophysics, Vol. 8, pp. 27-55.

Olson, P., Christensen, & U. R. (2006). Dipole Moment Scaling for Convection-Driven Planetary Dynamos. Earth and Planetary Science Letters, 250(3–4), 561–571. https://doi.org/10.1016/j.epsl.2006.08.008.

Oliveira, J. S., & Wieczorek, M. A. (2017). Testing the axial dipole hypothesis for the Moon by modeling the direction of crustal magnetization. Journal of Geophysical Research: Planets, 122(2), 383–399. https://doi.org/10.1002/2016JE005199 Oliveira

Panning, M. P., Kedar, S., Bowles, N., Calcutt, S., Cutler, J., Elliott, J. O., Garcia, R. F., Kawamura, T., Lognonné, P. H., Miller, E. A., Nunn, C., Pike, W. T., Pont, G., De Raucourt, S., Standley, I. M., Walsh, W., Weber, R. C., & Yana, C. (2021) Farside Seismic Suite (FSS): First seismic data from the farside of the Moon delivered by a commercial lander. American Geophysical Union Fall Meeting, Abstract #839546.

Pommier, A. (2018). Influence of sulfur on the electrical resistivity of a crystallizing core in small terrestrial bodies. *Earth and Planetary Science Letters*, *496*, 37–46. https://doi.org/10.1016/j.epsl.2018.05.032

Pommier, A., Davies, C. J., Zhang, R. (2020). A Joint Experimental-Modeling Investigation of the Effect of Light Elements on Dynamos in Small Planets and Moons. *Journal of Geophysical Research: Planets*, 125, e2020JE006492. https://doi.org/10.1029/2020JE006492

Roberts, P.H., 2007. Theory of the geodynamo. In: Schubert, G. (Ed.), Treatise on Geophysics, vol. 8. Core Dynamics. Elsevier, Amsterdam, pp. 67–105. Ch. 3. https://doi.org/10.1016/B978-044452748-6.00133-4.

Rückriemen, T., Breuer, D., & Spohn, T. (2015). The Fe snow regime in Ganymede's core: A deep-seated dynamo below a stable snow zone. Journal of Geophysical Research E: Planets, 120(6), 1095–1118. https://doi.org/10.1002/2014JE004781

Scheinberg, A., Soderlund, K. M., & Schubert, G. (2015). Magnetic field generation in the lunar core: The role of inner core growth. *Icarus*, *254*, 62–71. https://doi.org/10.1016/j.icarus.2015.03.013

Scheinberg, A. L., Soderlund, K. M., & Elkins-Tanton, L. T. (2018). A basal magma ocean dynamo to explain the early lunar magnetic field. *Earth and Planetary Science Letters*, *492*, 144–151. https://doi.org/10.1016/j.epsl.2018.04.015

Schubert, G. & Soderlund, K. M. (2011). Planetary magnetic fields: Observations and models. *Physics of the Earth and Planetary Interiors*, 187(3-4), 92-108. https://doi.org/10.1016/j.pepi.2011.05.013

Shimizu, H., Matsushima, M., Takahashi, F., Shibuya, H., & Tsunakawa, H. (2013). Constraint on the lunar core size from electromagnetic sounding based on magnetic field observations by an orbiting satellite. *Icarus*, *222*(1), 32–43. https://doi.org/10.1016/j.icarus.2012.10.029

Soderlund, K. M., & Stanley, S. (2020). The underexplored frontier of ice giant dynamos. *Philosophical Transactions of the Royal Society A*, *378*(2187), 20190479. https://doi.org/10.1098/rsta.2019.0479

Steenstra, E. S., Rai, N., Knibbe, J. S., Lin, Y. H., & van Westrenen, W. (2016). New geochemical models of core formation in the Moon from metal-silicate partitioning of 15 siderophile elements. Earth and Planetary Science Letters, 441, 1–9. https://doi.org/10.1016/j.epsl.2016.02.028

Steenstra, E. S., Agmon, N., Berndt, J., Klemme, S., Matveev, S., & Van Westrenen, W. (2018). Depletion of potassium and sodium in mantles of Mars,

Moon and Vesta by core formation. Scientific Reports, 8(1), 1–10. https://doi.org/10.1038/s41598-018-25505-6.

Stegman, D. R., Jellinek, A. M., Zatman, S. A., Baumgardner, J. R., & Richards, M. A. (2003). An early lunar core dynamo driven by thermochemical mantle convection. *Nature*, *421*(6919), 143–146. https://doi.org/10.1038/nature01267

Stevenson, D. J. (2003). Planetary magnetic fields. Earth and Planetary Science Letters, 208(1–2), 1–11. https://doi.org/10.1016/S0012-821X(02)01126-3

Stevenson, D. J. (1983). Planetary magnetic fields. *Reports on Progress in Physics*, *46*(5), 555–620. https://doi.org/10.1088/0034-4885/46/5/001

Stewart, A. J., Schmidt, M. W., Westrenen, W. Van, & Liebske, C. (2007). *Mars: A New Core-Crystallization Regime*. *316*(June), 1323–1326.

Stixrude, L., Scipioni, R., & Desjarlais, M. P. (2020). A silicate dynamo in the early Earth. *Nature Communications*, *11*(1), 6–10. https://doi.org/10.1038/s41467-020-14773-4

Strauss, B. E., Tikoo, S. M., Gross, J., Setera, J. B., & Turrin, B. (2021). Constraining the Decline of the Lunar Dynamo Field at ≈3.1 Ga Through Paleomagnetic Analyses of Apollo 12 Mare Basalts. Journal of Geophysical Research: Planets, 126(3), 1–21. https://doi.org/10.1029/2020JE006715

Stys, C., & Dumberry, M. (2020). A past lunar dynamo thermally driven by the precession of its inner core. *Journal of Geophysical Research: Planets*, *125*(7), e2020JE006396.

Tarduno, J. A., Cottrell, R. D., Lawrence, K., Bono, R. K., Huang, W., Johnson, C. L., Blackman, E. G., Smirnov, A. V., Nakajima, M., Neal, C. R., Zhou, T., Ibanez-Mejia, M., Oda, H., & Crummins, B. (2021). Absence of a long-lived lunar paleomagnetosphere. *Science Advances*, 7(32), 1–15. https://doi.org/10.1126/sciadv.abi7647

Tikoo, S. M., Weiss, B. P., Shuster, D. L., Suavet, C., Wang, H., & Grove, T. L. (2017). A two-billion-year history for the lunar dynamo. *Science Advances*, *3*(8), 1–10. https://doi.org/10.1126/sciadv.1700207

Warren, P. (1985). The Magma Ocean Concept and Lunar Evolution. *Annual Review of Earth and Planetary Sciences*, *13*(1), 201–240. https://doi.org/10.1146/annurev.ea.13.050185.001221

Weber, R. C., Lin, P. Y., Garnero, E. J., Williams, Q., & Lognonné, P. (2011). Seismic detection of the lunar core. *Science*, *331*(6015), 309–312. https://doi.org/10.1126/science.1199375

Weber, R., Neal, C. R., Grimm, R., Grott, M., Schmerr, N., Wieczorek, M., … Zuber, M. (2021). The scientific rationale for deployment of a long-lived geophysical network on the Moon. Bulletin of the AAS, 53(4). https://doi.org/10.3847/25c2cfeb.674dcfdf

Weiss, B. P., & Tikoo, S. M. (2014). The lunar dynamo. *Science*, *346*(6214). https://doi.org/10.1126/science.1246753

Wieczorek, M. A., Jolliff, B. L., Khan, A., Pritchard, M. E., Weiss, B. P., Williams, J. G., Hood, L. L., Righter, K., Neal, C. R., Shearer, C. K., McCallum, I. S., Tompkins, S., Hawke, B. R., Peterson, C., Gillis, J. J., & Bussey, B. (2006). The constitution and structure of the Lunar interior. *Reviews in Mineralogy and Geochemistry*, *60*(November), 221–364. https://doi.org/10.2138/rmg.2006.60.3

Wieczorek, M., Weiss, B., Breuer, D., Cébron, D., Fuller, M., Garrick-bethell, I., Gattacceca, J., Halekas, J., Hemingway, D., Hood, L., Wieczorek, M., Weiss, B., Breuer, D., Cébron, D., Fuller, M., Wieczorek, M. A., Weiss, B. P., Breuer, D., Cébron, D., & Fuller, M. (2022). *Lunar magnetism To cite this version : HAL Id : hal-03524536*.

Williams, J. G., Boggs, D. H., Yoder, C. F., Ratcliff, J. T., and Dickey, J. O. (2001), Lunar rotational dissipation in solid body and molten core, *J. Geophys. Res.*, 106(E11), 27933– 27968, doi:10.1029/2000JE001396.

Williams, Q. (2009). Bottom-up versus top-down solidification of the cores of small solar system bodies: Constraints on paradoxical cores. Earth and Planetary Science Letters, 284(3–4), 564–569. https://doi.org/10.1016/j.epsl.2009.05.019

Williams, J. G., Konopliv, A. S., Boggs, D. H., Park, R. S., Yuan, D. N., Lemoine, F. G., Goossens, S., Mazarico, E., Nimmo, F., Weber, R. C., Asmar, S. W., Jay Melosh, H., Neumann, G. A., Phillips, R. J., Smith, D. E., Solomon, S. C., Watkins, M. M., Wieczorek, M. A., Andrews-Hanna, J. C., … Zuber, M. T. (2014). Lunar interior properties from the GRAIL mission. *Journal of Geophysical Research: Planets*, *119*(7), 1546–1578. https://doi.org/10.1002/2013JE004559

Yin, Y., Li, Z., & Zhai, S. (2019). The phase diagram of the Fe-P binary system at 3 GPa and implications for phosphorus in the lunar core. *Geochimica et Cosmochimica Acta*, *254*, 54–66. https://doi.org/10.1016/j.gca.2019.03.037

Zhan, X., & Schubert, G. (2012). Powering Ganymede's dynamo. *Journal of Geophysical Research E: Planets*, *117*(8), 1–7. https://doi.org/10.1029/2012JE004052

Ziegler, L. B., & Stegman, D. R. (2013). Implications of a long-lived basal magma ocean in generating Earth's ancient magnetic field. *Geochemistry, Geophysics, Geosystems*, *14*(11), 4735–4742. https://doi.org/10.1002/2013GC005001

APPENDIX A. RADIAL STRUCTURE OF THE LUNAR CORE

We approximated the lunar core as a mixture of liquid Fe and liquid Fe-10 wt% S to make structure models. We followed the procedure detailed in Khan et al. (2017), especially in their Appendix A, to calculate radial profiles of

density, pressure, and temperature. We use the mass-weighted averages of the depth-dependent values of the Grüneisen parameter and the coefficient of thermal expansion. We then performed a least-squares fit to parameterize the radial density using a fourth-degree polynomial:

$$\rho(r) = \rho_0 \left[1 - \left(\frac{r}{L_\rho} \right)^2 - A_\rho \left(\frac{r}{L_\rho} \right)^4 \right], \qquad (A1)$$

where ρ_0 is density at the center of the core, L_ρ is a length scale, and A_ρ is a constant. The effective bulk modulus is then $K_0 = 2\pi G (L_\rho \rho_0)^2/3$, where G is the gravitational constant. The derivative of the effective bulk modulus is $K_1 = (10\ A_\rho + 13)/5$. Finally, the adiabatic thermal gradient in the core is then $T_a(r) = T(0)[\rho(r)/\rho_0]^\gamma$.

APPENDIX B. ENERGETICS OF A DYNAMO IN THE LUNAR CORE

Section 2.2 describes the heat budget of the lunar core. For completeness, we list here the polynomial equations used to calculate the different terms. Analogous equations that were developed to model Earth's core can be found in Labrosse (2015), albeit with slightly different notation and additional complexities added to the analytic formulation, and in the Supporting Information for Blaske & O'Rourke (2021).

In our models, the total heat flow across the core/mantle boundary can be partitioned into four different terms, each of which is proportional to the overall cooling rate of the core (dT_{CMB}/dt). First, we have the heat flow associated with secular cooling of the fluid portion of the core. Before the inner core nucleates, we have

$$\tilde{Q}_S = -\frac{4}{3}\pi\rho_0 C_C L_\rho^3 f_c\left(\frac{R_C}{L_\rho}, \gamma\right)\left[1 - \left(\frac{R_C}{L_\rho}\right)^2 - A_\rho\left(\frac{R_C}{L_\rho}\right)^4\right]^{-\gamma}, \qquad (B1)$$

where

$$f_c(x,\delta) = x^3\left[1 - \frac{3}{5}(\delta+1)x^2 - \frac{3}{14}(\delta+1)(2A_\rho - \delta)x^4\right]. \qquad (B2)$$

After the inner core nucleates,

$$\tilde{Q}_S = -\frac{4}{3}\pi\rho_0 C_C L_\rho^3\left[1 - \left(\frac{R_I}{L_\rho}\right)^2 - A_\rho\left(\frac{R_I}{L_\rho}\right)^4\right]^{-\gamma}\left[\frac{dT_L}{dR_I} + \frac{2\gamma T_L(R_I)\left(\frac{R_I}{L_\rho^2}\right)\left(1 + 2A_\rho\left(\frac{R_I}{L_\rho}\right)^2\right)}{1 - \left(\frac{R_I}{L_\rho}\right)^2 - A_\rho\left(\frac{R_I}{L_\rho}\right)^4}\right]\left[f_c\left(\frac{R_C}{L_\rho}, \gamma\right)\right.$$

$$\left. - f_c\left(\frac{R_I}{L_\rho}, \gamma\right)\right]\left(\frac{dR_I}{dT_C}\right), \qquad (B3)$$

where $T_L(R_I)$ is the liquidus temperature evaluated at the inner core boundary given by

$$T_L(R_I) = T_L(0) - K_0\left(\frac{dT_L}{dP}\right)\left(\frac{R_I}{L_\rho}\right)^2 + \frac{c_0}{f_c\left(\frac{R_C}{L_\rho}, 0\right)}\left(\frac{dT_L}{dc}\right)\left(\frac{R_I}{L_\rho}\right)^3. \quad (B4)$$

Here c_0 is the mass fraction of sulfur in the outer core, which increases as the inner core grows. Differentiating this equation yields the slope of the liquidus at the inner core boundary:

$$\frac{dT_L}{dR_I} = -2K_0\left(\frac{dT_L}{dP}\right)\left(\frac{R_I}{L_\rho^2}\right) + \frac{3c_0}{f_c\left(\frac{R_C}{L_\rho}, 0\right)}\left(\frac{dT_L}{dc}\right)\left(\frac{R_I^2}{L_\rho^3}\right). \quad (B5)$$

Following Nimmo (2015), we use this slope and the adiabatic thermal gradient to calculate the growth rate of the inner core

$$\frac{dR_I}{dT_C} = -\frac{1}{\left(\frac{dT_L}{dP} - \frac{dT_a}{dP}\right)_{R_I}}\left(\frac{T_L(R_I)}{T_{CMB}\rho(R_I)g(R_I)}\right). \quad (B6)$$

The growth of the inner core also releases latent heat

$$\tilde{Q}_L = 4\pi R_I^2 \rho(R_I) T_L(R_I) \Delta S_C \left(\frac{dR_I}{dT_C}\right), \quad (B7)$$

where ΔS_C = 200 J/K/kg is the entropy of melting for the inner core (Nimmo 2015). Next, we compute the gravitational energy related to the exclusion of sulfur from the inner core as it freezes:

$$\tilde{Q}_G = \frac{8\pi^2 G \rho_0 c_0 \alpha_I R_I^2 L_p^2}{f_c\left(\frac{R_C}{L_\rho}, 0\right)}\left[f_\chi\left(\frac{R_C}{L_\rho}\right) - f_\chi\left(\frac{R_I}{L_\rho}\right)\right]\left(\frac{dR_I}{dT_C}\right), \quad (B8)$$

where α_I = 2.3 is the coefficient of compositional expansion for enriching the outer core in sulfur (Nimmo 2015). Here we leverage another useful function:

$$f_\chi(x) = x^3\left\{-\frac{1}{3}\left(\frac{R_I}{L_\rho}\right)^2 + \frac{1}{2}\left[1 + \left(\frac{R_I}{L_\rho}\right)^2\right]x^2 - \frac{13}{70}x^4\right\}. \quad (B9)$$

Last and easiest, the radiogenic heat in the core is

$$Q_R = M_C H_K [K] \exp(-\lambda_K t), \quad (B10)$$

where λ_K = 1.76 × 10^{-17} s^{-1} and H_K = 4.2 × 10^{-14} W/kg/ppm are the decay constant and the heat production rate at t = 0 for potassium-40, respectively.

The energy budget by itself does not reveal whether a dynamo may exist in the lunar core. We must compute the dissipation budgets, again following Labrosse (2015) and studies such as Blaske & O'Rourke (2021). First, we expand equation 3 in the main text as

$$\Phi_{CMB} = \left(\frac{T_D[T_L(R_I) - T_{CMB}]}{T_L(R_I)T_{CMB}}\right)Q_L + \left(\frac{T_D}{T_{CMB}}\right)Q_G + \left(\frac{T_D - T_{CMB}}{T_{CMB}}\right)Q_R + \left(\frac{T_D(T_S - T_{CMB})}{T_S T_{CMB}}\right)Q_S - \Phi_K. \quad (B11)$$

Here we use the average temperature in the outer core:

$$T_D = \frac{T(R_I)}{\left[1 - \left(\frac{R_I}{L_\rho}\right)^2 - A_\rho \left(\frac{R_I}{L_\rho}\right)^4\right]^\gamma} \left[\frac{f_c\left(\frac{R_C}{L_\rho}, 0\right) - f_c\left(\frac{R_I}{L_\rho}, 0\right)}{f_c\left(\frac{R_C}{L_\rho}, -\gamma\right) - f_c\left(\frac{R_I}{L_\rho}, -\gamma\right)}\right], \quad (B12)$$

The effective temperature associated with dissipation from secular cooling is almost identical to T_D but slightly hotter:

$$T_S = \frac{T(R_I)}{\left[1 - \left(\frac{R_I}{L_\rho}\right)^2 - A_\rho \left(\frac{R_I}{L_\rho}\right)^4\right]^\gamma} \left[\frac{f_c\left(\frac{R_C}{L_\rho}, \gamma\right) - f_c\left(\frac{R_I}{L_\rho}, \gamma\right)}{f_c\left(\frac{R_C}{L_\rho}, 0\right) - f_c\left(\frac{R_I}{L_\rho}, 0\right)}\right]. \quad (B13)$$

Finally, we can calculate the dissipation sink associated with the thermal conductivity of the core fluid:

$$\Phi_K = 16\pi\gamma^2 k_C L_\rho \left[f_k\left(\frac{R_C}{L_\rho}\right) - f_k\left(\frac{R_I}{L_\rho}\right)\right] T_D, \quad (B14)$$

where our last useful function is

$$f_k(x) = 0.2x^5\left[1 + \frac{10}{7}(1 + 2A_\rho)x^2 + \frac{5}{9}(3 + 10A_\rho + 4A_\rho^2)x^4\right]. \quad (B15)$$

Note that we can then write the total adiabatic heat flow in terms of Φ_K:

$$Q_{AD} = \left(\frac{T_S T_{CMB}}{T_D(T_S - T_{CMB})}\right)\Phi_K \quad (B16)$$

which is an energy-based definition that is basically equivalent to the usual formula, $Q_{AD} \sim 4\pi R_C^2 k_C (dT_a/dr)$, derived from Fourier's law.

APPENDIX C. MAGNETIC DIFFUSION TIME

We determine the time it takes for the field to decay after convection ceases following the procedure detailed in Stevenson (2003) to approximate the magnetic diffusion time:

$$\tau = \frac{{R_C}^2}{\pi^2 \lambda}. \quad (C1)$$

Here R_C is radius of the electrically conducting region (i.e., the core) and λ is magnetic diffusivity given by:

$$\lambda = \frac{1}{\mu_0 \sigma}, \quad (C2)$$

where μ_0 is the permeability of free space and σ is the electrical conductivity. We assume $\lambda \sim 1$ m^2/s, appropriate for terrestrial planets with a liquid iron alloy core (e.g., Schubert and Soderlund 2011), such that the magnetic field will diffuse across the core in $\tau \sim 400$ years.

APPENDIX D: TABLES

Table D1
Description of Model Constants

Term	Description	Value
μ_0	Permeability of free space	1.257×10^{-6} H·m^{-1}
G	Gravitational constant	6.67×10^{-11} m^3·kg^{-1}·s^{-2}
R	Universal gas constant	8.3145 J·K^{-1}·mol^{-1}
R_M	Radius of the Moon	1737 km
R_C	Radius of the core	350 km
Ω	Angular velocity of the Moon	2.66×10^{-6} rad·s^{-1}
K_0	Effective modulus	121.4×10^9 Pa
K_1	Effective derivative of effective modulus	5.7871
A_ρ	Constant in density profile	1.59
ρ_0	Central density	6477 kg·m^{-3}
P_0	Central pressure	5.15×10^9 Pa
M_C	Mass of the core	1.16×10^{21} kg
V_C	Volume of the core	3.95×10^{16} m^3
g	Gravitational acceleration near the core-mantle boundary	0.6311 m·s^{-2}
γ	Grüneisen parameter for the core	1.65
C_c	Specific heat of the core	835 J·kg^{-1}·K^{-1}
ΔS_C	Entropy of melting for the inner core	200 J·K^{-1}·kg^{-1}
α_I	Coefficient of compositional expansion for enriching the outer core in sulfur	2.3
λ_K	Average decay constant for potassium-40	1.76×10^{-17} s^{-1}
H_K	Heat production rate for potassium-40	4.2×10^{-14} W·kg^{-1}·ppm^{-1}
c	Constant of proportionality in equations 5–7	0.63
dT_L/dc	Compositional dependence of liquidus temperature	−2500 K
dT_L/dP	Pressure dependence of liquidus temperature	3×10^{-8} K·Pa^{-1}

Table D2

Definition of Model Inputs and Outputs

Variable	Definition	Values
Input parameters		
[S]	Abundance of sulfur in the core[a]	1–6 wt%
[K]	Abundance of potassium in the core[b]	0–50 ppm
k_C	Thermal conductivity of the core[c]	10–50 W m^{-1} K^{-1}
Q_C	Present-day heat flow across the core-mantle boundary[d]	0–2 GW
Energy budget outputs of the core		
Q_{CMB}	Heat flow across the core-mantle boundary	GW
Q_L	Latent heat from inner core nucleation	GW
Q_G	Gravitational energy released from inner core nucleation	GW
Q_R	Radiogenic heating in the core	GW
Q_S	Secular cooling of the core	GW
Entropy budget outputs of the core		
Φ_{CMB}	Dissipation available to power a dynamo	MW
Φ_L	Dissipation associated with latent heat	MW
Φ_G	Dissipation associated with gravitational energy	MW
Φ_R	Dissipation associated with radiogenic heating	MW
Φ_S	Dissipation associated with secular cooling	MW
Φ_K	Dissipation sink associated with thermal conductivity	MW

[a]Weber et al. 2011.

[b]Laneuville et al. 2014, Scheinberg et al. 2015, Hirose et al. 2013.

[c]Pommier 2018.

[d]Laneuville et al. 2014.